Static membrane action in restrained RC beams: Experimental investigation, and numerical and analytical prediction

Citation for the original published paper (version of record):

Lozano Mendoza, F., Johansson, M., Leppänen, J. et al (2026). Static membrane action in restrained RC beams: Experimental investigation, and numerical and analytical prediction. Journal of Building Engineering, 129.
http://dx.doi.org/10.1016/j.jobe.2026.116768

(article starts on next page)

Journal of Building Engineering 129 (2026) 116768

Contents lists available at ScienceDirect

Journal of Building Engineering

journal homepage: www.elsevier.com/locate/jobe

Static membrane action in restrained RC beams: Experimental investigation, and numerical and analytical prediction

Fabio Lozano [a,*], Morgan Johansson [a,b], Joosef Leppänen [a], Mario Plos [c]

[a] Division of Structural Engineering, Chalmers University of Technology, Gothenburg, SE-41296, Sweden
[b] Norconsult Sverige AB, Gothenburg, SE-41755, Sweden
[c] Swedish Transport Administration, Gothenburg, SE-41104, Sweden

A R T I C L E I N F O

Keywords:
Restrained RC beam
Membrane action
Catenary action
FEM
Analytical model
Internal strain energy

A B S T R A C T

Membrane action can substantially enhance the resistance and deformation capacity of restrained reinforced concrete (RC) elements, offering critical additional capacity for elements subjected to impulsive loading. However, its practical utilization remains limited, largely due to the absence of a consistent, simplified approach capable of describing the full structural response. This study conducted experimental investigation of membrane action in six longitudinally and rotationally restrained RC beams subjected to static three-point bending. The specimens varied in slenderness, reinforcement ratio, and fracture strain of the reinforcement. All beams exhibited combined flexural and membrane action, with an enhanced peak resistance attributable to compressive membrane action (CMA). Clear differences in reinforcement fracture and cracking development were observed in the post-peak response across the specimens, reflecting the influence of geometry, reinforcement properties and boundary conditions. The results showed that CMA contributed significantly to the energy absorption capacity of specimens with lower slenderness or lower reinforcement ratios, while more slender beams with reinforcement with higher fracture strain benefited primarily from tensile membrane action (TMA). Reinforcement fracture during the CMA phase was observed in some specimens, underscoring the need for predictive methods that explicitly account for this phenomenon. Two simplified approaches for predicting the full load–deflection response were also presented: a finite element (FE) model and an analytical approach extending an existing framework. The FE model showed good agreement with the experimental results, accurately capturing peak resistance and reinforcement fracture. The analytical model provided satisfactory predictions, particularly during the CMA phase.

1. Introduction

Restrained reinforced concrete (RC) beams and slabs are normally designed using yield line theory by assuming a collapse mechanism governed by the formation of plastic hinges. This approach considers only the bending moment at the critical sections and—provided that brittle shear failure is prevented—offers a reliable estimate of the load-carrying capacity when no in-plane membrane forces are present. However, RC elements are rarely isolated. Their behaviour is influenced by boundary conditions (BCs) imposed by adjacent structural components, which may restrain both their horizontal translation and rotation. Such restraint

* Corresponding author.
E-mail address: Fabio.Lozano@chalmers.se (F. Lozano).

https://doi.org/10.1016/j.jobe.2026.116768
Received 6 March 2026; Received in revised form 5 June 2026; Accepted 30 June 2026
Available online 1 July 2026

induces membrane forces within the element, potentially increasing its ultimate resistance and deformation limit. Restrained RC elements generally exhibit two distinct consecutive response phases. Initially, compressive membrane action (CMA), or arching action, develops. At larger deflections—typically exceeding the section depth—the element transitions into tensile membrane action (TMA), or catenary action. Both mechanisms are widely recognised to enhance the flexural capacity compared with equivalent unrestrained elements [1].

The restraint imposed by the BCs becomes relevant once cracking initiates. As the neutral axis shifts towards the compression zone due to cracking, the resulting net axial extension would naturally cause the element's ends to move outwards. However, this outward movement is restrained by the BCs, generating compressive membrane forces and initiating the CMA phase. The peak resistance in this phase, P_{CMA}, may significantly exceed the flexural capacity of an equivalent unrestrained system, P_{flex}. Beyond this peak, the resistance decreases with increasing deflection until the membrane force reduces to zero. At this point, the ends begin to move inwards. If the reinforcement is adequately anchored, tensile axial force develops and the element transitions into the TMA phase. Early in this phase, bending action may still contribute to the resistance. However, as cracking penetrates the full section depth, the load is carried predominantly by the reinforcement through catenary action. Moreover, the load-carrying capacity continues increasing with deflection until catastrophic reinforcement failure is reached.

It is important to note that the reinforcement in different sections or layers may fracture at different deflections before system collapse, which is usually reflected as sudden discrete drops in the load-deflection curve. Smith [2] distinguished between two stages within the TMA regime: (i) *primary* catenary action, which is defined as TMA behaviour prior to fracture of the extreme tension reinforcement; and (ii) *secondary* catenary action, which begins after this reinforcement fracture (if the element is doubly reinforced).

Despite the well-documented enhancement in the capacity of restrained RC elements compared with their unrestrained counterparts, practical application of membrane action in normal design situations is limited [3]. Several factors contribute to this, including uncertainties regarding the actual boundary conditions of the elements within the structure, the fact that full development of TMA involves large deflections and considerable damage, and the lack of a universally accepted design model of sufficient simplicity and accuracy. Nevertheless, this additional capacity could be highly valuable in extreme loading scenarios, for which more uncertain design assumptions may be justified and severe damage may be accepted provided that outright collapse is prevented. Typical examples of such scenarios include blast loading, impact events, and accidental column removals. In such cases, the ability to safely dissipate energy is a desired property in the affected structure. Such energy absorption capacity is proportional to the element's resistance and deformation limit. Membrane action may improve both of these parameters. This suggests that more efficient and economical solutions may be achievable for structures required to withstand extreme dynamic actions if their membrane action is properly understood and utilised.

Ockleston [4] was among the first to explicitly recognize the potential of membrane action in RC structures. Ockleston's work initiated a period of intensive research on the topic that continued into the early 1980s. Key contributions from this era include those of Park [5–7], Keenan [8], and Black [9]. Much of the research during this period focused on two-way slabs subjected to uniform loading. Interest in membrane action in RC elements was revived in the early 2000s, largely driven by concerns related to structural robustness and emergency load redistribution. Smith [2] provides a comprehensive review of the research conducted up to 2016 and also reports an extensive experimental study on catenary action in RC slabs. In the past decade, research has expanded to encompass a wider range of structural systems, including hollow core elements [10], precast concrete beam–column sub-assemblages [11], and beam-slab substructures [12,13], as well as studies examining membrane action in the context of fire safety [14]. More recent work has further advanced the field. Cui et al. [15] examined RC beams under a combined membrane and shear mechanism and proposed an improved resistance function for this response mode. Shaik et al. [16] employed experimental and numerical methods to investigate the influence of tensile membrane action on the combined failure of RC beam-slab systems. In addition, Jiang et al. [17] examined the progressive collapse resistance of curved beam-column systems, considering the influence of arching and catenary action on their structural response.

Despite the extensive body of research on membrane action in RC structures, several important limitations remain. First, most experimental studies have examined elements with large span-to-depth ratios (L/h), often within the context of progressive collapse scenarios where a two-span beam becomes a long single-span element after middle column loss. Consequently, there is a need for further investigation on membrane action in beams and one-way slabs that are single-span by design. A recent study addressing lower span-to-depth ratios ($L/h < 15$) is that of Cui et al. [15]. However, their specimens exhibited shear damage, limiting the applicability of their findings to members governed primarily by flexural behaviour. Su et al. [18] provided another valuable contribution, but the reinforcement used in their test specimens had fracture strains exceeding 26%, much higher than the typical fracture strains of modern European reinforcement. This highlights a broader issue: much of the earlier experimental work used highly ductile reinforcing steel with elongation capacities well above the requirements in current standards, such as Eurocode 2 [19]. Furthermore, as noted by Smith [2], existing research on catenary action predominantly addresses *primary* catenary behaviour, while *secondary* catenary action remains comparatively underexplored. Finally, only a limited number of studies have explicitly examined the energy absorption associated with membrane action, despite its importance for structures subjected to extreme dynamic loading.

The prediction of the response of restrained RC elements has also received considerable attention. Several analytical and numerical models have been developed, either to estimate the ultimate resistance or to construct the full load-deflection relationship. Both response phases, CMA and TMA, are typically treated separately. Analytical models describing CMA are commonly based on plastic hinge idealizations. Among these, the model proposed by Park [5] remains one of the most widely recognised and has served as the foundation for other subsequent developments [20–24]. For instance, Kang and Tan [20] established a relationship between reinforcement strain and global deflection and expanded the model to account for the constitutive laws of concrete, reinforcement and engineering cementitious composites. Recent contributions focusing on beam-like elements include Zhu et al. [25], who developed an analytical approach for predicting the resistance of restrained one-way slabs subjected to point loading, accounting for variable section depth and different degrees of rotational restraint. In addition, Chen et al. [26] introduced a theoretical model for clamped hybrid fibre-reinforced concrete beams subjected to uniform loading, which can also be employed for elements constructed with conventional concrete.

Analytical models for predicting the response under TMA are typically derived from equilibrium of an assumed catenary mechanism. By neglecting concrete tensile strength and assuming that all reinforcement has yielded, the resistance can be expressed as a function of the deflection and membrane force. For one-way systems, this leads to relatively simple formulations. The same general approach can be applied to both *primary* and *secondary* catenary action by appropriately defining the effective reinforcement stress and area for each stage. Among the existing models, Park's formulation [7] for uniformly loaded two-way rectangular slabs remains one of the most widely used and forms the basis for guidelines in design manuals such as UFC 3-340-02 [27]. More recent developments include, for instance, the models reported in Refs. [28,29].

Some researchers have proposed models capable of describing the entire load-deflection curve of restrained RC elements, encompassing both CMA and TMA. Pham and Tan [30] introduced a semi-analytical approach in which the overall behaviour of beam–column sub-assemblages subjected to a point load is represented using a piecewise multi-linear resistance curve. Kang et al. [13] presented an integral analytical approach to describe the behaviour of beam-slab configurations exhibiting both arching action and catenary action. Monserrat-López et al. [31] proposed a method based on limit analysis, supported on examination of an experimental database and detailed finite element (FE) analyses, which incorporates both CMA and TMA. Cui et al. [32] evaluated CMA and TMA in restrained RC beams subjected to uniformly distributed loading using separate formulations, while also providing recommendations for constructing a complete load-deflection curve suitable for simplified dynamic analysis of structural elements subjected to blast loading.

Despite the wide range of available analytical approaches, some important gaps remain. A key limitation is that most existing analytical models for the CMA phase do not account for reinforcement fracture, even though such phenomena has been reported in the literature [2,33,34]. Even in analytical models addressing the TMA phase, reinforcement fracture is typically treated in a simplified manner, often by assuming a reduced effective reinforcement area. These simplifications hinder the development of reliable resistance functions and introduce inaccuracies in the evaluation of the internal strain energy, both of which are essential for accurately characterising the dynamic response and energy absorption capacity of structural elements subjected to impulsive loading.

In addition to analytical and semi-analytical models, several numerical approaches with varying levels of complexity have been proposed [33,35–39]. These numerical approaches can typically capture the response with great accuracy. However, they are often relatively complex and difficult to implement in practice. For this reason, there is a clear need for validated simplified models that can be implemented using commercially available FE software, bridging the gap between advanced research tools and practical engineering applications.

This paper presents an experimental investigation of membrane action in longitudinally and rotationally restrained RC beams subjected to three-point bending. The study examined specimens with varying span-to-depth ratios, reinforcement ratios, and reinforcement ductility. The experimentally measured internal strain energy was compared with theoretical predictions based on Eurocode 2 and UFC 3-340-02. In addition, the study presents two simplified approaches for estimating the full load–deflection response and the associated membrane forces: a numerical FE model and an analytical method. The FE model, implemented on ABAQUS/Standard [40], was deliberately kept simple and general to facilitate its practical implementation on different commercial FE tools. The analytical approach was based on the framework developed by Kang and Tan [20]. The study is limited to RC specimens with symmetrical, continuous reinforcement subjected to three-point bending.

2. Experimental program

This study is part of a larger research campaign for investigating the impact response of restrained RC beams. This paper presents the results and evaluation of the static tests (labelled with odd numbers). The remaining specimens were subjected to impact loading. The results of the impact tests will be presented in future publications.

Table 1
Description of the test specimens.

Specimen	h	b	L/h	L/d [a]	Longitudinal reinforcement (mm)		ρ (%)		Stirrups
	(mm)	(mm)	(–)	(–)	Top	Bottom	Top	Bottom	(mm)
B1	100	200	20.0	26.0	2ø6	2ø6	0.39	0.37	40ø6@50
B3	100	200	20.0	26.3	2ø8	2ø8	0.71	0.66	40ø6@50
B5	100	200	20.0	26.0	2ø6	2ø6	0.39	0.37	6ø6@50 [b]
B7	100	200	20.0	26.3	2ø8	2ø8	0.71	0.66	6ø6@50 [b]
B9	160	200	12.5	15.2	2ø6	2ø6	0.21	0.21	25ø6@80
B11	160	200	12.5	15.3	2ø8	2ø8	0.38	0.38	25ø6@80

[a] Calculated with d at midspan.
[b] Stirrups were introduced only in a limited region at midspan.

2.1. Description of the specimens

The study investigated the behaviour of six longitudinally and rotationally restrained RC beams subjected to static three-point bending. The beams were monolithically cast with strong column stubs. Although referred to as beams throughout this paper for convenience, the specimens were intended to represent strips of cast-in-situ RC slabs. The primary target span-to-depth ratio was 20, which is typical for RC slabs; in addition, two specimens with a span-to-depth ratio of 12.5 were included in the study. Given these ratios, the specimen dimensions—clear span $L = 2.0$ m and width $b = 0.2$ m—were determined considering the capacity of the reaction frames. The geometry and reinforcement layout are presented in Table 1 and Fig. 1, in which h is the section depth and ρ is the reinforcement ratio. The RC beams were symmetrically reinforced with continuous reinforcement anchored within the column stubs. Four specimens were provided with shear reinforcement (closed stirrups) along their entire length, while the remaining two beams had shear reinforcement only in a limited region around the loading plate (intended to prevent local failure in the impact zone in the second phase of the overall research campaign). The reinforcement layout was designed to promote ductile behaviour. The specimens complied with Eurocode 2's minimum longitudinal and—where relevant—shear reinforcement amounts. The column stubs were provided with sufficient reinforcement to minimize cracking during testing.

2.2. Test setup

The column stubs were vertically supported on compression load cells mounted on steel footings. Teflon sheets were used between the concrete surface and the load cells to minimize the horizontal reaction force on the steel footings. To provide longitudinal and rotational restraint at the specimens' ends, the column stubs were connected to braced steel frames by a pair of horizontal pinned steel links. The steel frames were bolted to the strong RC floor. The horizontal reaction force was transferred to the floor by means of friction between the steel frames and concrete floor. Tension/compression load cells were installed on each horizontal link at the left-hand support to measure the horizontal reaction forces. For the same purpose, strain gauges were installed on the surface of the connection links at the right end. No additional out-of-plane constraints were incorporated in the test setup. Fig. 2 shows the general setup of the experiments. Fig. 3 shows additional relevant details of the test setup.

The point load was applied on the top surface at midspan by a displacement-controlled hydraulic actuator. A steel loading plate with dimensions 120 × 120 × 12 mm was used between the actuator and the concrete surface. The load was applied at a rate of 2 mm/min until a deformation of 10 mm was reached. From that point, the loading rate was gradually increased until a final rate of 10 mm/min. The applied load and the midspan deflection were measured simultaneously using a load cell and a displacement gauge. The load was applied until the specimen collapsed.

To complement the measurements obtained from the gauges and load cells, the response of the specimens was also examined using Digital Image Correlation (DIC). DIC enables measurement of deflections and rotations as well as evaluation of crack propagation by tracking the relative deformation of a speckle pattern applied to the beam surface across a sequence of digital photographs captured during testing. A three-dimensional (3D) setup was employed using a *pair* of cameras—collectively referred to as Camera 1 in Figs. 2 and 3—positioned at different angles relative to the speckle pattern. The cameras recorded at a rate of 30 frames/minute. To achieve a suitable balance between spatial resolution and field of view, Camera 1 covered only slightly more than half the specimen's length, including the column stub. The speckle pattern was created by first painting the surface white and then manually applying randomised black spots with a brush. To support the main DIC analysis, a second camera (Camera 2 in Fig. 2) was used to record the entire beam at a rate of 1 frame/minute, allowing detection of any non-symmetric response. The 3D DIC system also enabled monitoring of the out-of-plane motion, which was confirmed to be negligible.

During testing, the right-hand support frame displayed larger-than-expected horizontal translations. Therefore, different measures were progressively introduced to increase the translational stiffness of the supports (the beams were tested in numerical order). The ground bolts were also re-tightened between tests. Specimens B1 and B3 were tested using the original setup shown in Fig. 2. After first

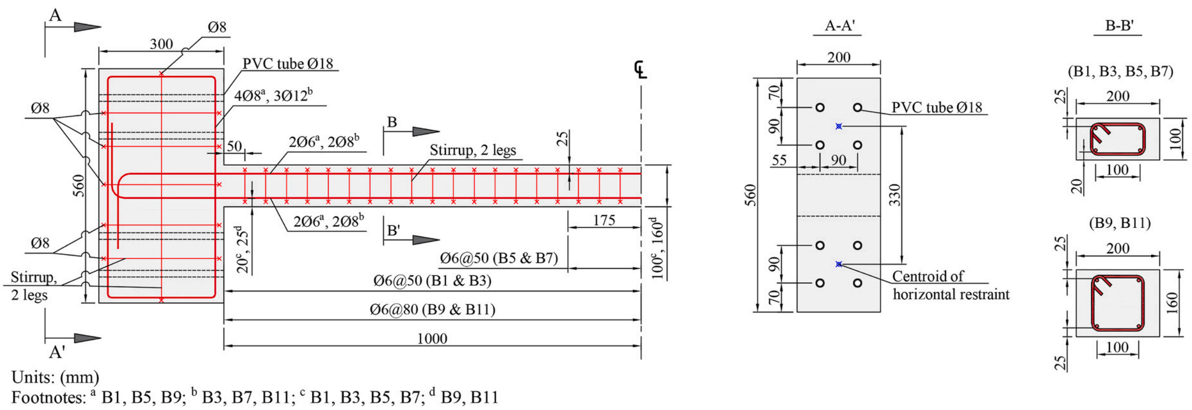

Fig. 1. Geometry and reinforcement layout of the test specimens. Because of symmetry, only half the specimen is shown.

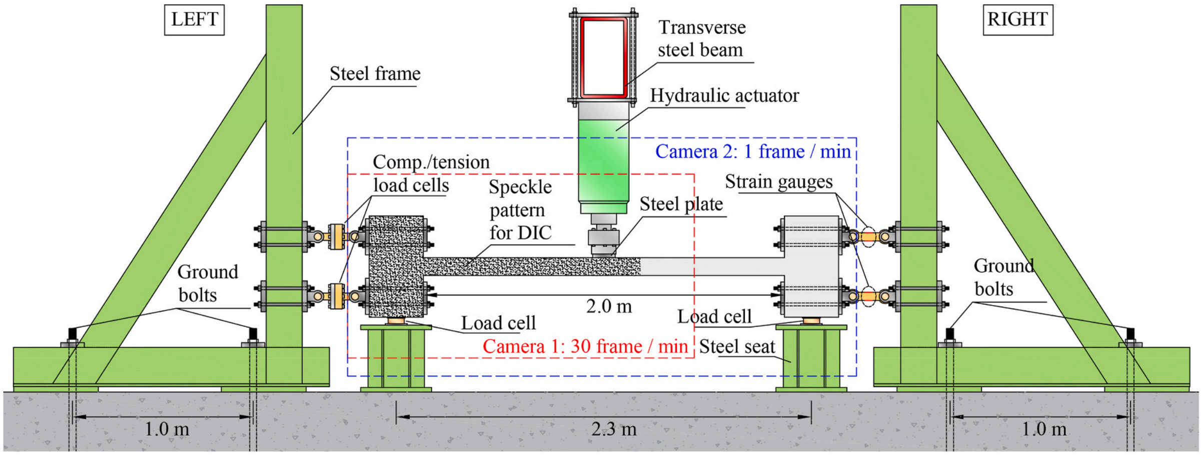

Fig. 2. General schematic description of the test setup.

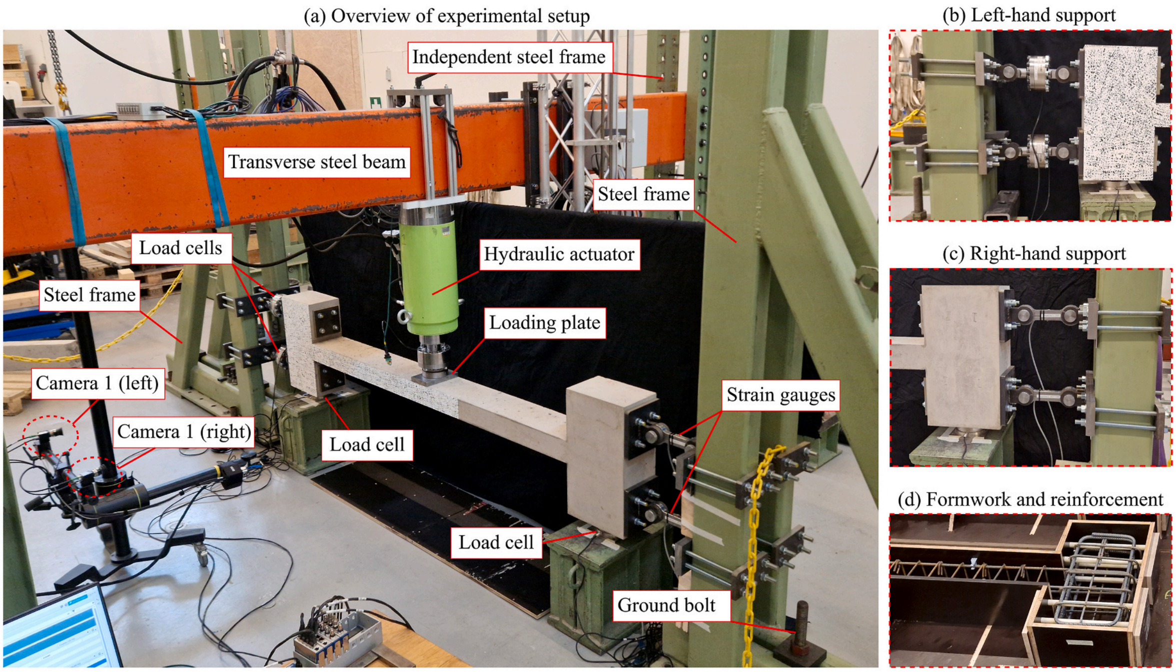

Fig. 3. Overall image of the test setup and close-up views of key components.

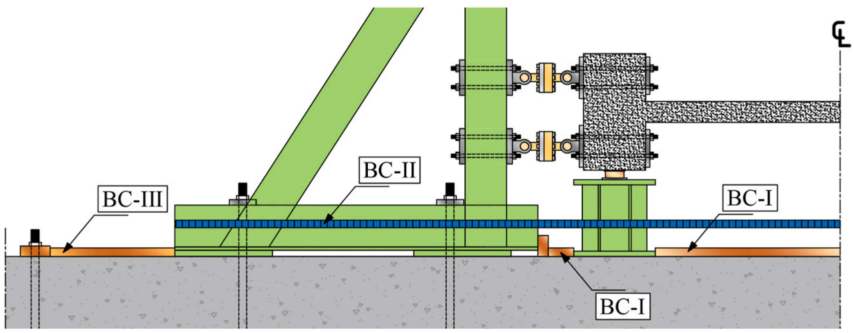

Fig. 4. Modifications to the boundary conditions during testing.

detecting significant inward displacement at the right-hand support (on the order of 15 mm), steel plates were installed between the reaction frames (BC-I in Fig. 4) before testing B5 to further restrain their relative inward movement. However, the results for B5 indicated that outward translation was also significant, albeit to a lesser extent. Thus, a ratchet strap was added to minimize this outward displacement for specimens B7 and B9 (BC-II in Fig. 4). Despite these measures, the support translations remained asymmetric. Therefore, for specimen B11, steel plates were bolted to the floor on the outside of the frames (BC-III in Fig. 4), providing a more robust restraining system. The significance of this is that all specimens were tested under different boundary conditions. Due to the substantial influence of the BCs on the response, care was taken to describe the behaviour of the supports in detail. This is treated in Section 3.3.

2.3. Material properties

Material tests were conducted on both the concrete and the reinforcement bars. For the concrete, the mean compressive cube strength, $f_{cm,cube}$, and the mean split tensile strength, f_{sp}, were determined experimentally using cubic specimens (150 × 150 × 150 mm) of the same age as the tested beams (>110 days). Other relevant material parameters were estimated from these experimental values in accordance with Eurocode 2 and Model Code 2010 [41]. According to the tests, $f_{cm,cube} = 67.0$ MPa and $f_{sp} = 4.2$ MPa. Using Eq. (1), the mean cylinder compressive strength, f_{cm}, was estimated as 55.0 MPa. Similarly, the mean uniaxial tensile strength, f_{ctm}, was estimated as 3.8 MPa using Eq. (2).

$$f_{cm} = 0.82 \cdot f_{cm,cube} \qquad \text{Eq. (1)}$$

$$f_{ctm} = 0.9 \cdot f_{sp} \qquad \text{Eq. (2)}$$

Ribbed reinforcement bars of class 500C were used. Random samples were taken for both diameters (6 and 8 mm) and tested in tension in a universal testing machine. Fig. 5 gives the experimental stress-strain curves for different rebar samples. The reinforcing steel with 6 mm diameter was stored in coils and straightened up before delivery. Because of this process, its stress-strain curve resembled the typical curve of cold-worked steel, in which no clear yield plateau could be discerned. Hence, the yield strength of the ø6-mm rebars was defined as the proof stress $f_{0.2}$. A summary of the relevant mechanical properties of the reinforcing steel is given in Table 2, in which f_y is the yield strength, f_u is the ultimate strength, ε_u is the strain at which f_u occurs, and E_s is the module of elasticity.

3. Experimental results

3.1. Cracking pattern in the tested specimens

Fig. 6 shows the condition of the beams immediately before outright collapse. The response of all specimens was governed by flexural action, with major flexural cracks at midspan and both supports. No clear evidence of shear cracks was observed, even in the specimens without stirrups outside the midspan region (B5 and B7).

In specimens B3, B5, and B7, the cracked region at the right support featured two major cracks of comparable width, accompanied by concrete spalling on the compressed side. This damage mechanism may be associated to the unexpectedly large horizontal translation recorded at the right support. In contrast, damage at the left support was in general dominated by a single primary crack. This indicates that the rotational demand distributed over a longer cracked zone at the right support, enabling an increased rotational capacity at that support. Indeed, as described in Section 3.2, most beams experienced fracture of the tension reinforcement at the left support before any rebar fracture occurred at the right support.

Fig. 7 presents contour plots of major strains—used to visualise cracking development—for three selected specimens. At the peak CMA resistance, P_{CMA}, the specimens exhibited a similar pattern: vertical cracks initiating from the bottom fibre at midspan, and vertical cracks initiating from the top surface near the support. At the stage of bottom-reinforcement fracture at midspan (M.B), the crack at the location of rebar fracture widened substantially, while adjacent bottom cracks either reduced in width or closed entirely. In

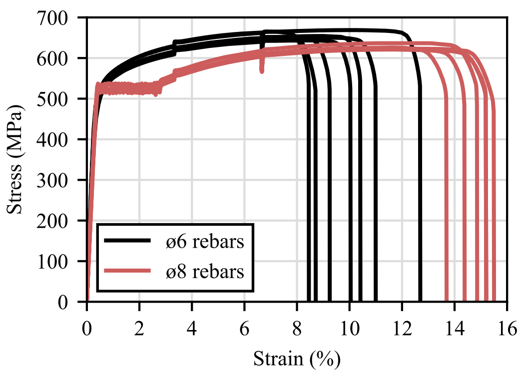

Fig. 5. Experimental stress-strain relationship of the reinforcement bars as a function of the diameter.

Table 2
Mechanical properties of the reinforcing steel.

Diameter (mm)	f_y (MPa)	f_u (MPa)	f_u/f_y (−)	ε_u (%)	E_s (GPa)
6	525	655	1.25	8.2	188
8	523	625	1.20	11.8	188

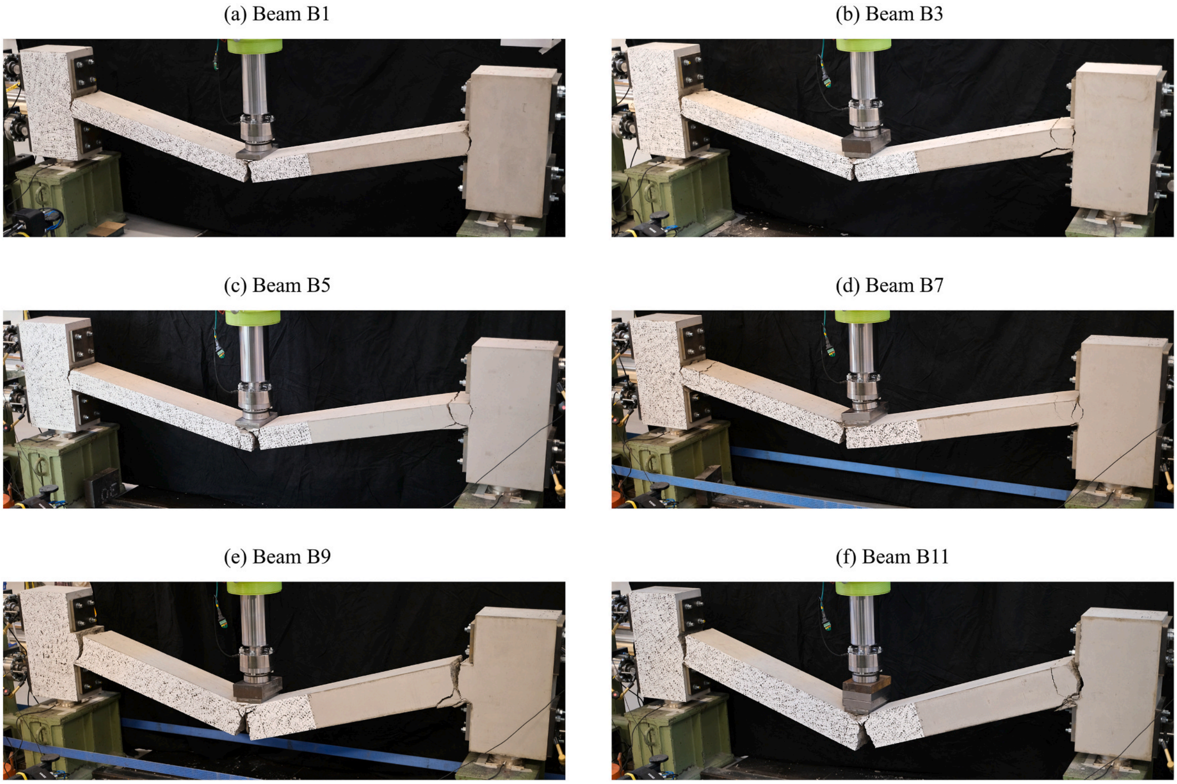

Fig. 6. Damage in the test specimens right before outright collapse.

contrast, new cracks opened at the top surface, indicating that the hogging moment dominated the bending contribution. In B3 and B7, these new top cracks also appeared very close to the loading point. Beyond this stage, the cracking patterns diverged. Specimen B3 experienced top-reinforcement fracture at the support (L.T), after which the load was carried predominantly by catenary action. This is reflected in the cracks penetrating the full section depth and becoming uniformly distributed along the span. However, specimen B7 retained its top reinforcement at the support. As a result, the support moment capacity continued to contribute even at large deflections, meaning that the load was partially carried through cantilever action. Consequently, the cracks were markedly wider near the top and appear to not have fully crossed the section depth, although they still distributed relatively uniformly along the span. Specimen B11 also experienced top-reinforcement fracture at the support (L.T). However, unlike B3, only a few cracks were open near the support and midspan region at this stage. Top-reinforcement fracture at the support in B11 occurred during the CMA phase, which suggests that the compressive membrane force prevented more cracks from opening.

3.2. Load-deflection curves

The recorded applied load and horizontal reaction force are shown in Fig. 8 for all specimens. The effect of the self-weight was removed from the plots in Fig. 8. The self-weight did not induce membrane forces in the beams, as they rested on the vertical supports before the longitudinal restraint was applied. The figure also indicates the deflections at which reinforcement fracture events occurred as well as the theoretical flexural capacity of the beams, P_{flex}. The flexural capacity was calculated with Eq. (3), in which $M_{Rd,1}$ and $M_{Rd,2}$ are the moment capacities at the support and midspan determined assuming the simplified rectangular stress block in Eurocode 2 and neglecting any axial force. Only minor differences were observed between the horizontal reaction forces measured with the load cells (left end) and those obtained from the strain gauges (right end). Thus, the horizontal reaction force presented in Fig. 8 corresponds to the average value recorded at both ends. During testing of specimens B3 and B11, the actuator reached its maximum permissible extension. In these cases, the tests were temporary halted, the actuator retracted, and additional steel plates were installed

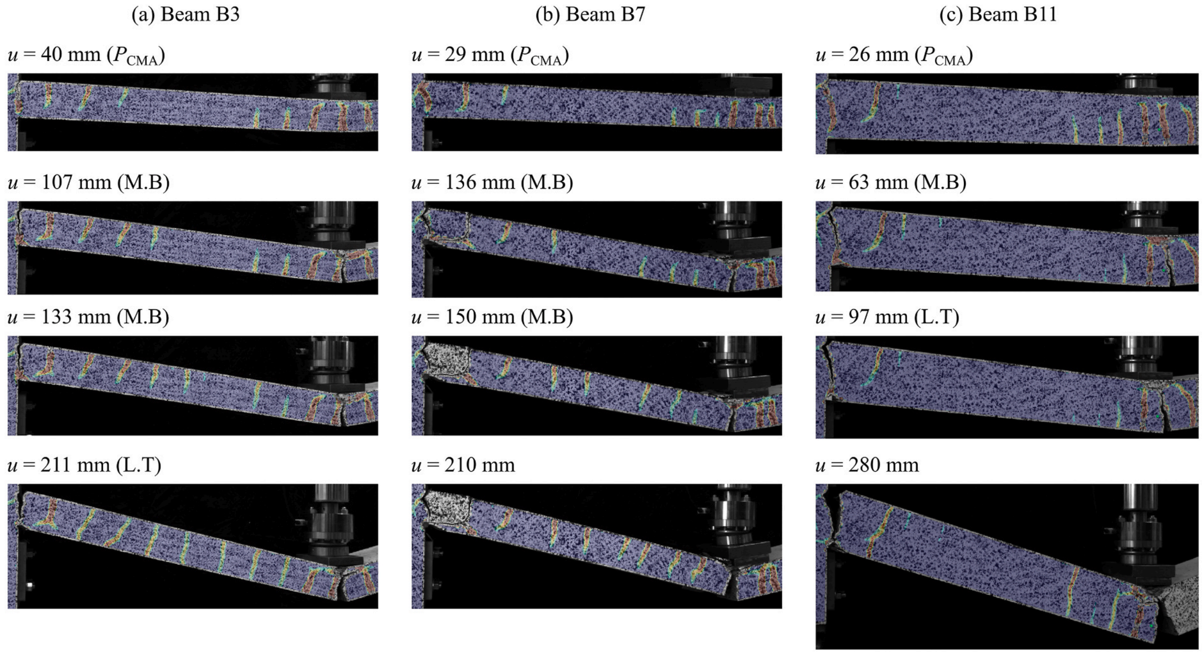

Fig. 7. Major strains from DIC analysis in selected specimens at different midspan deflections (u). M.B and L.T denote bottom-reinforcement fracture at midspan and top-reinforcement fracture at the left support.

on top of the loading plate. The tests were then resumed and continued until failure of the specimen. Based on the continuity of the response after resuming the tests, it was judged that this procedure had no significant effect on the overall response.

$$P_{\text{flex}} = \frac{4\left(M_{\text{Rd},1} + M_{\text{Rd},2}\right)}{L} \qquad \text{Eq. (3)}$$

Table 3 shows key experimental values, in which P_{CMA} and P_{TMA} are the maximum applied load within the CMA and TMA phases, H_{CMA} and H_{TMA} are the maximum horizontal reaction forces in each phase, and $H_{\text{CMA, corr}}$ is the corresponding horizontal reaction force at P_{CMA}.

Inspection shows that the development of compressive membrane forces during the initial part of the response resulted in an enhanced resistance compared with pure flexural capacity. The enhancement of the resistance during the CMA response ranged between 1.18 and 1.92, as shown in Table 3. It should be noted that the uncertainties associated with the calculation of P_{flex} are carried over into the estimation of the enhancement ratio. The enhancement was greatest in beams with $L/h = 12.5$ (B9 and B11). The maximum load-carrying capacity during the TMA phase exceeded the peak CMA resistance in B3 and B7, but it was markedly lower in the remaining beams. This suggests that the CMA phase is more prominent in beams with low slenderness, while TMA is the primary response in more slender beams with larger reinforcement ratio and higher-ductility reinforcement.

The specimens with $h = 160$ mm (B9 and B11) experienced fracture of the extreme tension reinforcement at the midspan and support sections during the CMA phase, before the snap-through behaviour could be completed. This led to a sudden loss of capacity, attributed to an instability mechanism triggered by the combined effect of (i) the loss of moment capacity following fracture of the tension reinforcement and (ii) the high compressive membrane force within the element at that instant. As a result, the beams dropped abruptly by 34 mm (B9) and 50 mm (B11), causing them to lose contact with the hydraulic actuator. The discontinuity observed in the load-deflection curves in Fig. 8(e) and (f) corresponds to this sudden drop. However, the tests could be resumed afterwards, with the load carried by *secondary* catenary action. That is, no *primary* catenary action was mobilised in these specimens. It should be noted that, although the response observed after reloading may not typically be utilised in conventional design scenarios, it can still provide a meaningful contribution to the energy absorption capacity under impulsive loading scenarios.

In specimens with $h = 100$ mm and ø8-mm rebars (B3 and B7), snap-through occurred without any significant loss of load-carrying capacity and no rebar fracture took place during the CMA phase. In contrast, in specimens with $h = 100$ mm and ø6-mm rebars (B1 and B5), first fracture of tension reinforcement occurred almost simultaneously with the transition to TMA. This behaviour was attributed to both the lower reinforcement ratio and the smaller fracture strain in these beams. It was also observed that the resistance at the lowest point of the snap-through is comparable or slightly smaller than the theoretical flexural capacity without axial force.

It is important to highlight the observed risk for fracture of one or more tension reinforcement layers during the CMA phase or near the CMA-to-TMA transition. This indicates that accurately predicting this phenomenon is essential; otherwise, the TMA capacity may be significantly overestimated. Analytical and numerical models must then be capable of capturing the onset of early rebar fracture for a reliable estimate of the TMA response.

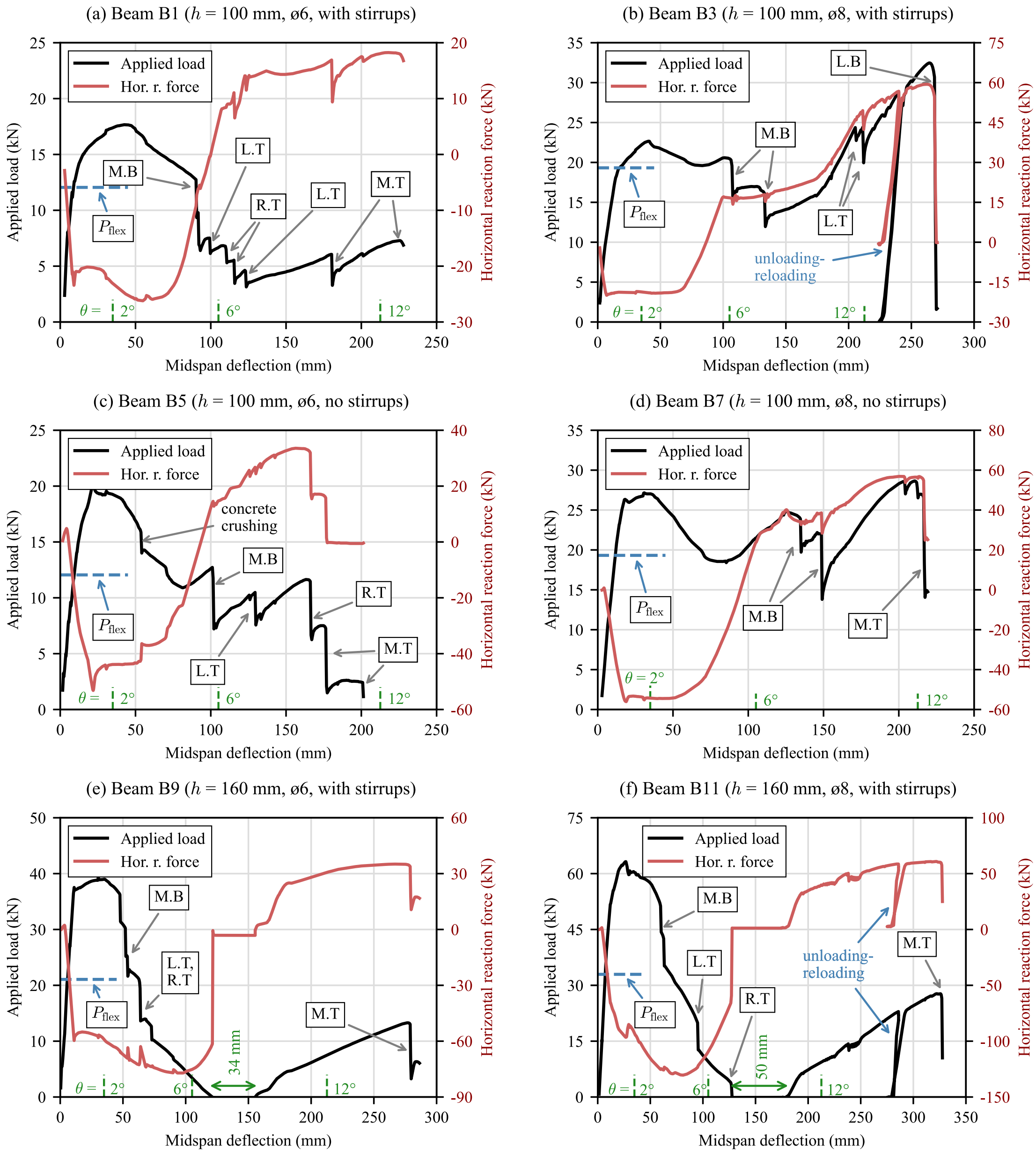

Fig. 8. Experimentally measured applied vertical load and horizontal reaction force. Location of rebar fracture is given by M.B (midspan, bottom), M.T (midspan, top), L.B (left end, bottom), L.T (left end, top), and R.T (right end, top). P_{flex} is the flexural resistance without axial force. θ is the support rotation.

Table 3
Experimentally measured values within the CMA and TMA phases.

Beam	P_{CMA} (kN)	P_{TMA} (kN)	P_{flex} (kN)	$P_{\text{CMA}}/P_{\text{flex}}$ (–)	$P_{\text{TMA}}/P_{\text{flex}}$ (–)	H_{CMA} (kN)	$H_{\text{CMA, corr}}$ (kN)	H_{TMA} (kN)
B1	17.7	7.3	12.1	1.46	0.60	−26.2	−24.8	18.2
B3	22.7	32.5	19.3	1.18	1.68	−20.0	−19.0	59.4
B5	19.6	12.7	12.1	1.62	1.05	−53.2	−45.6	33.6
B7	27.2	28.6	19.3	1.41	1.48	−56.1	−55.2	56.9
B9	39.4	13.3	21.1	1.87	0.63	−77.2	−58.2	35.1
B11	63.2	27.8	33.0	1.92	0.84	−130.4	−96.6	60.9

In all specimens, first rebar fracture happened in the bottom reinforcement at midspan. This aligns with the findings by Smith [2], who reported first rebar fracture at the same location in symmetrically reinforced slab strips. This could potentially be explained by an initial free rotation at the supports (meaning that field moment develops before any support moment), strain penetration into the column stubs, or the extended cracked zone near the supports observed in some specimens (which increased the rotational capacity at the supports).

In beams B1, B5, B9 and B11, the initial fracture of the bottom reinforcement at midspan was followed by fracture of the top reinforcement at one or both beam ends. Thereafter, *secondary* catenary action was sustained solely by the remaining reinforcement layers that were initially in compression. Final collapse occurred when the top reinforcement at midspan eventually fractured.

Specimen B3 exhibited a different failure sequence. Following fracture of the bottom reinforcement at midspan, both the top and bottom reinforcement at the left support fractured, while no reinforcement fracture occurred at the right support. Furthermore, B3 was the only specimen in which the top reinforcement at midspan remained intact throughout the test. Inspection of Fig. 7(a) indicates that, at the instant of fracture of the top reinforcement at the left support ($u = 211$ mm), the crack width at midspan was comparable to that at the support. This contrasts with the other specimens, for which the major crack at midspan was noticeably wider than those near the supports. These observations suggest that the conditions governing rotational capacity at midspan were more favourable in B3, thereby preventing fracture of the top reinforcement at that location.

Specimen B7 displayed yet another failure pattern: only the reinforcement at midspan fractured (both at the top and bottom), whereas all rebars at the supports remained intact. The absence of reinforcement fracture at both ends in B7—and at the right support in B3—is likely connected to the formation of multiple major cracks at these supports. These multiple cracks likely reduced strain concentration and enhanced the rotational capacity, thereby preventing fracture. The underlaying cause of this cracking pattern cannot be conclusively determined from the results of the present study. However, it may be related to the complex nonlinear boundary conditions in these beams caused by the unexpected slip observed at the right support. The boundary conditions are discussed in detail in Section 3.3.

The presence or absence of shear reinforcement does not seem to have significantly affected the response of the more slender beams. Hence, under this assumption, the effect of the compressive membrane force on the peak CMA resistance can be examined by comparing specimens B1 and B5. Specimen B1 reached $P_{\mathrm{CMA}} = 17.7$ kN, whereas B5—nominally identical but without stirrups outside the midspan region—reached $P_{\mathrm{CMA}} = 19.6$ kN. The corresponding horizontal reactions forces at P_{CMA} were -24.8 kN and -45.6 kN. This means that an 84% increase in compressive axial force in B5 resulted in only an 11% increase in P_{CMA}. A similar trend was observed for specimens B3 and B7, which achieved $P_{\mathrm{CMA}} = 22.7$ kN and $P_{\mathrm{CMA}} = 27.2$ kN, associated with a horizontal reaction force of -19.0 kN and -55.2 kN, respectively. In other words, a 190% increase in compressive axial force produced only a 20% increase in peak resistance. These results indicate a positive relationship between the compressive membrane force and P_{CMA}. However, a substantial increase in compressive normal force does not translate into a proportionally large increase in peak CMA resistance.

3.3. Translational and rotational stiffness at the supports

As outlined in Section 2.2, the translational stiffness of the support frames was progressively adjusted during testing. Consequently, an accurate characterisation of the BCs is essential for a complete and reliable description of the specimens' response. The properties of the BCs were established by examining the relationship between the measured horizontal force and the corresponding displacement at the outer face of the column stubs. On the left-hand side, the displacement was obtained using DIC applied to the speckle pattern captured by Camera 1. On the right-hand side, no speckle pattern was available. Instead, DIC was used to track the motion of the bolts and nuts in the steel connections using images from Camera 2. A comparison of DIC measurements from Cameras 1 and 2 on the left-hand side confirmed that tracking the bolted connection with Camera 2 produced results of similar accuracy with errors on the order of ± 1 mm.

Inspection of Fig. 8 shows that the horizontal restraint exhibited a nonlinear response in most beams. In compression, the horizontal reaction force increased approximately linearly until a threshold was reached, after which sliding at the right-hand support began. A peak in the horizontal force (corresponding to the transition from static to kinetic friction) is clearly visible in the horizontal force-deflection curves of specimens B1 through B9. For some specimens, the horizontal force continued to rise even after sliding initiated, possibly because the steel frame encountered a region on the floor that allowed for greater friction force. In the tensile phase,

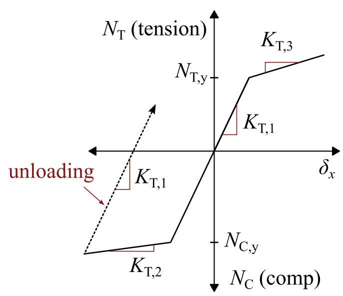

Fig. 9. Schematic description of the translational stiffness at the right support.

specimens B1, B3 and B7 also experienced a plateau in the horizontal force, during which deflection increased without a corresponding rise in horizontal reaction force. For B3 and B7, the right-hand support regained its stiffness after a certain horizontal displacement, after which the horizontal force continued increasing.

The results indicate that the left-hand BCs can be idealised as fully linear elastic, characterised by a translational stiffness K_T and a rotational stiffness K_R. In contrast, the right-hand BCs are more complex and exhibit a nonlinear, plastic-like behaviour, as illustrated in Fig. 9. The limits $N_{C,y}$ and $N_{T,y}$ denote the compressive and tensile horizontal forces at which sliding of the steel frame initiates. As noted earlier, for some specimens the reaction force continued increasing after sliding of the steel frame started. This secondary effect was incorporated by adjusting the stiffness constants $K_{T,2}$ and $K_{T,3}$. A summary of the stiffness properties is given in Table 4. It should be noted that the rotational stiffness was not considerably affected by the translation at the right support. Thus, an average value was adopted for both supports. Finally, a small initial "gap" in the test setup was also detected. This "gap" represents the deformation needed for the multiple components in the restraining system to fully engage. Similar gaps have been previously reported in comparable setups [20]. For simplicity, the initial gap was assumed to be concentrated on the right support.

3.4. *Evaluation of the internal strain energy*

RC members subjected to impulsive loading are designed to provide sufficient flexural resistance and ductility so that the work done by the load can be resisted through the internal strain energy. Therefore, the test specimens were evaluated in terms of their strain energy. By the principle of energy conservation, the total strain energy, E_{tot}, can be calculated by integrating the load-deflection curve up to collapse using Eq. (4). Here, E_{CMA} is the energy dissipated during the CMA phase, E_{TMA} is the energy absorbed during the TMA regime, u_0 is the deflection at the CMA-to-TMA transition, and u_{max} is the ultimate deflection at final reinforcement fracture.

$$E_{tot} = E_{CMA} + E_{TMA} = \int_0^{u_0} P\,du + \int_{u_0}^{u_{max}} P\,du \qquad \text{Eq. (4)}$$

Although the ability to resist the imparted work is the desired outcome, the most common design-controlling criterion for impulsively loaded RC members is a deformation limit, which is typically expressed in terms of support rotations. According to UFC 3-340-02 [27], the support rotation of unrestrained blast-loaded RC slabs failing in bending is limited to 2° and 6° in members without and with shear reinforcement, respectively. Restrained shear-reinforced slabs may be designed for an ultimate support rotation of 12°.

Eurocode 2 prescribes a plastic rotational capacity, $\theta_{EC,pl}$—applicable to members with and without shear reinforcement—as a function of the concrete and reinforcement class and the x_u/d ratio, in which x_u denotes the compressive zone's height in the ultimate limit state. This capacity corresponds to the rotation at a double-sided plastic hinge at the position of the applied point load. Therefore, when the point load acts at midspan, Eurocode 2's rotational capacity must be divided by two to obtain the corresponding support rotation. It is also important to note that Eurocode 2's plastic rotational capacity refers to the rotation at ultimate flexural resistance. That is, it is no intended to describe the rotation at system collapse nor does it account for TMA response.

Table 5 presents the experimentally determined values of E_{tot}, E_{CMA}, and E_{TMA}, along with the support rotation at outright collapse, θ_{tot}. To enable a fair comparison with the deformation limit prescribed in Eurocode 2, the energy dissipated up to peak CMA resistance, $E_{P,CMA}$, and the corresponding support rotation, $\theta_{P,CMA}$, were also determined.

The design criteria specified by Eurocode 2 and UFC 3-340-02, originally expressed in terms of allowable rotations, were converted into equivalent strain energy and are presented in Table 5. The strain energy associated with Eurocode 2's plastic rotational capacity, E_{EC}, was calculated by assuming a bilinear load-deflection response, in which the load increases linearly from zero to P_{flex}, and thereafter remains constant up to the support rotation $\theta_{EC,tot} = \theta_{el} + \theta_{EC,pl}$, in which θ_{el} is the elastic rotation. The elastic stiffness was determined by Eq. (5), in which I_{II} is the moment of inertia of the cracked concrete section and E_c is the concrete's modulus of elasticity.

$$K_{II} = \frac{192 E_c I_{II}}{L^3} \qquad \text{Eq. (5)}$$

The strain energy corresponding to the UFC 3-340-02's rotation limits was calculated with a similar bilinear idealisation, but with the response integrated up to a total support rotation of 2° ($E_{UFC,2}$), 6° ($E_{UFC,6}$), and 12° ($E_{UFC,12}$), respectively. In addition, the flexural resistance was determined following the procedure in UFC 3-340-02, which requires assuming cross-section type II and III (i.e. concrete assumed not effective in resisting moment) for the calculations of $E_{UFC,6}$ and $E_{UFC,12}$. The provisions in UFC 3-340-02 for

Table 4
Properties of the experimental boundary conditions.

Beam	Left end	Right end						Both ends
	Translation	Translation					Gap	Rotation
	K_T (N/m)	$K_{T,1}$ (N/m)	$N_{C,y}$ (kN)	$K_{T,2}$ (N/m)	$N_{T,y}$ (kN)	$K_{T,3}$ (N/m)	(mm)	K_R (Nm/rad)
B1	9.3×10^7	3.1×10^8	22	1.1×10^6	16	2.0×10^5	0.3	5.4×10^6
B3	6.7×10^7	7.4×10^7	19	1.6×10^6	19	1.3×10^6	0.1	4.5×10^6
B5	5.1×10^7	6.7×10^7	48	2.4×10^6	---	---	0.8	1.8×10^6
B7	1.0×10^8	7.9×10^7	55	2.8×10^6	35	5.6×10^6	0.6	2.0×10^7
B9	1.0×10^8	1.2×10^8	57	1.9×10^6	---	---	0.8	9.9×10^6
B11	9.5×10^7	3.0×10^7	---	---	---	---	0.6	1.1×10^7

Table 5
Evaluation of the support rotation and corresponding strain energy.

Beam	Experiment								Eurocode 2			UFC 3-340-02		
	$E_{P,CMA}$	$\theta_{P,CMA}$	E_{CMA}	E_{TMA}	E_{CMA}	E_{TMA}	E_{tot}	θ_{tot}	E_{EC}	$\theta_{EC,tot}$	$E_{EC,N}$	$E_{UFC,2}$	$E_{UFC,6}$	$E_{UFC,12}$
	(Nm)	(°)	(Nm)	(Nm)	(%)	(%)	(Nm)	(°)	(Nm)	(°)	(Nm)	(Nm)	(Nm)	(Nm)
B1	593	2.43	1396	687	0.67	0.33	2083	12.71	347	1.93	402	---	742	1470
B3	694	2.32	1647	3791	0.30	0.70	5438	14.83	490	1.74	515	---	1251	2451
B5	439	1.76	1346	865	0.61	0.39	2211	10.77	347	1.93	441	308	742	1470
B7	588	1.77	1985	2886	0.41	0.59	4871	11.88	490	1.74	556	524	1251	2451
B9	950	1.74	2389	993	0.71	0.29	3382	13.55[a]	398	1.25	744	---	1458	3003
B11	1179	1.53	4409	2350	0.65	0.35	6759	15.00[b]	696	1.37	1050	---	2510	5113

[a] A rotation corresponding to 34 mm was subtracted, see Fig. 8(e).
[b] A rotation corresponding to 50 mm was subtracted, see Fig. 8(f).

determining the design reinforcement stress and the equivalent elastic stiffness were also respected.

The total strain energy in the specimens reinforced with ø8-mm rebars was clearly greater than that in beams with ø6-mm rebars. This is a consequence of both the increased resistance due to the larger reinforcement ratio and the larger fracture strain of the ø8-mm rebars. The latter delays reinforcement fracture, allowing more effective utilization of the TMA capacity. Indeed, in specimens B3 and B7, E_{TMA} accounted, on average, for 64% of the total strain energy. These were the only specimens that benefitted substantially from both *primary* and *secondary* catenary action. In contrast, in beams with lower slenderness or with reinforcement with lower fracture strain, the greatest contribution to the total strain energy came from CMA. E_{CMA} was, on average, 64% for B1 and B5, and 68% for B9 and B11. In these beams, fracture of at least one extreme tension reinforcement layer occurred during the CMA phase or almost simultaneously with the onset of TMA, meaning that E_{TMA} was mostly due to *secondary* catenary action. It is also noteworthy that E_{tot} was lower in B9 compared to B3 and B7, which highlights that a greater load-carrying capacity does not necessarily translate into greater energy absorption capacity. Additionally, beams B1 and B3—which developed comparatively smaller compressive membrane forces due to the reduced restraint at the right support—reached P_{CMA} at a larger rotation, $\theta_{P,CMA}$. As a result, $E_{P,CMA}$ was greater in these beams than in B5 and B7, respectively, despite having lower P_{CMA}.

In general, the rotational capacity and strain energy determined using Eurocode 2 ($\theta_{EC,tot}$ and E_{EC}) were lower than the corresponding experimental values ($\theta_{P,CMA}$ and $E_{P,CMA}$). Among these two quantities, the prediction of rotational capacity showed better agreement with the experiments. Indeed, reasonable estimates were obtained for specimens B5 and B7, although Eurocode 2's provisions underestimated the rotational capacity by approximately 10 to 28% for the remaining specimens. Greater discrepancies were observed in the prediction of energy absorption capacity in those beams.

It is important to note that no compressive membrane force was originally considered in the calculations with Eurocode 2. While consideration of this force may improve accuracy, estimating it is non-trivial and no method is explicitly provided by the standard. Nonetheless, to assess its influence, this study incorporated the experimentally measured compressive membrane force corresponding to P_{CMA} (given in Table 3) into the calculations with Eurocode 2. This adjustment produced a modified rotational capacity and corresponding strain energy, $E_{EC,N}$, the latter of which is reported in Table 5. The updated strain energy shows improved agreement with the experimental values, with discrepancies reduced to between 1 and 32%.

The smallest strain energy value based on the UFC 3-340-02's provisions, $E_{UFC,2}$, applies to elements without stirrups. Thus, this would be the rotation limit imposed on specimens B5 and B7. However, contrary to the assumption in UFC 3-340-02, these beams did not exhibit a reduced rotational capacity compared to B1 and B3. This indicates that the absence of stirrups in the region close to the supports did not restrict their deformation capacity in the manner implied by the provisions in UFC 3-340-02.

For restrained shear-reinforced beams, UFC 3-340-02 specifies a support rotation limit of 12°. In general, this threshold appears reasonable, as only two beams failed at support rotations slightly below 12°. Moreover, the corresponding strain-energy estimate, $E_{UFC,12}$, provided the closest approximation to the experimental results. Nevertheless, the strain energy was underestimated for all specimens, indicating a general *bias* in the prediction. Understanding this bias requires examining the original studies on which the UFC 3-340-02's 12°-rotation limit is based. Smith [2] traced the origin of this limit to several studies from the previous century, including [7–9]. Examination of those studies revealed that the tests were terminated either before reinforcement fracture or at first extreme tension reinforcement fracture. In other words, as noted by Smith [2], the measured capacity corresponded only to *primary* catenary action. In contrast, all specimens in the present study were loaded until final reinforcement fracture, meaning that *secondary* catenary action also contributed to the determined energy absorption capacity. This alone explains much of the systematic underprediction. In addition, the UFC 3-340-02's provisions neglect the contribution of arching action, which accentuates this difference.

Beyond the general bias, the error in the predictions showed certain dependency to the slenderness and the combined effect of the reinforcement ratio and fracture strain. When grouped by span-to-depth ratio, the error was consistently greater in beams with higher span-to-depth ratios. Likewise, when grouped by reinforcement diameter, the error was greater in beams with ø8-mm reinforcement—which implies greater reinforcement ratio and fracture strain. This behaviour may be related to the characteristics of the specimens in the aforementioned original studies, which consisted predominantly of elements with span-to-depth ratios markedly greater than 12.5 and highly ductile reinforcement. Importantly, this should not necessarily be interpreted as the prediction improving with decreasing slenderness or reinforcement ductility. Rather, the effect of these two factors appears to act opposite to the general bias, partially compensating for it, and thus reducing the overall error.

It is also worth noting that, because UFC 3-340-02's method assigns a fixed rotational capacity, it predicts a greater energy absorption capacity for specimen B9 compared to B3 and B7. This contradicts the experimental results, which show that B9 developed lower strain energy than B3 and B7.

Taken together, these results suggest that estimating the available strain energy solely from the 12°-rotation limit may be overly simplistic, as it does not enable consideration of other potential key factors, such as the span-to-depth ratio or the reinforcement's properties.

4. Numerical and analytical evaluation of membrane action

The present study developed two different approaches to predict the response of restrained RC beams subjected to three-point bending: a numerical FE model and an analytical model. FE models generally enable higher-fidelity predictions and allow utilization of advanced features, such as nonlinear boundary conditions and bond-slip behaviour. However, they also introduce additional challenges, including the need for specialised software, solving convergence issues, and conducting mesh sensitivity analyses. In contrast, the analytical model is intended as a practical and efficient tool for predicting the load-deflection curve, making it particularly suitable for preliminary design stages and parametric studies. Moreover, such as a model can be readily incorporated into broader analytical frameworks, e.g. simplified two-degree-of-freedom systems for analysing the impact response of restrained RC beams.

4.1. FE model

4.1.1. Overview

The nonlinear FE model was implemented in ABAQUS/Standard [40]. The modelling strategy was deliberately kept simple to facilitate reproduction in other FE software equipped with general plasticity material models. The beam length was set equal to the clear span between the inner faces of the column stubs. The concrete part was represented using Timoshenko beam elements (type B21), with the cross-section discretised with 51 section points. The reinforcement bars were modelled using truss elements (type T2D2). Instead of modelling each individual bar, a single truss element was used at the top and bottom, with an equivalent area equal to the sum of the respective rebars. Fig. 10 shows the geometry of the model.

The boundary conditions were implemented using connector elements. Translational restraint was provided through AXIAL connectors. At the left support, the connector was assigned linear-elastic behaviour. At the right support, nonlinear plastic behaviour, as given in Fig. 9, was included in the connector properties. The initial axial gap was modelled entirely at the right end using AXIAL connectors with nonlinear elasticity. Rotational restraint at both supports was introduced through linear-elastic connectors of type ROTATION.

The bond between the concrete and the rebars was modelled using combined connectors of type CARTESIAN + ROTATION. The bond-slip behaviour was defined according to the model in Model Code 2010 [41]. This model has been successfully employed in previous studies concerned with membrane action in RC structures [42,43]. Pull-out failure with *good bond* conditions was assumed. Thus, the maximum bond stress, τ_{bmax}, was set to 18.5 MPa. The other parameters, s_1, s_2, α, and τ_{bf}—as defined in Model Code 2010—were set to 1.0 mm, 2.0 mm, 0.4, and $0.4\tau_{bmax}$, respectively. The clear distance between ribs, s_3, was measured as 5 mm. Plasticity properties were assigned in the main direction of the rebars to represent the bond-slip relationship, while the connection was assumed fully rigid in the remaining directions. The effective bond force was computed by multiplying the bond stress with the effective surface area of the rebars. The connection between the ends of the rebars and the node at the BCs was implemented using rigid connectors.

A mesh sensitivity analysis was conducted to evaluate three mesh sizes: 50, 100, and 200 mm. For each mesh size, the softening behaviour of the material models was regularised according to Section 4.1.2. Similar results were obtained for the models with mesh size of 50 and 100 mm. Thus, the mesh size was set to 100 mm.

A deformation-controlled load was applied at the midspan node. The analysis was continued until outright collapse was reached. The total computation time was under 5 min using a single CPU.

4.1.2. Material models

The behaviour of the concrete material was modelled using the Concrete Damaged Plasticity (CDP) model including compressive behaviour, plasticity and tensile behaviour. Damage evolution was omitted to keep the model as simple and computationally efficient as possible. A detailed description of the implementation of this material model for RC beams can be found in Ref. [44].

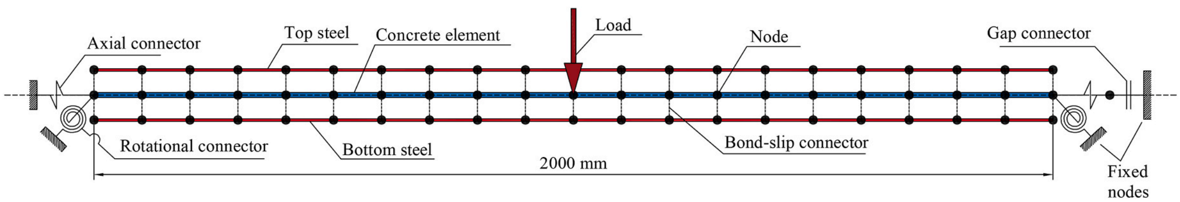

Fig. 10. Schematic description of the FE model.

The behaviour of concrete in compression up to the limiting strain $\varepsilon_{c,lim}$ was defined using the model from Model Code 2010. To describe the post-peak softening behaviour beyond $\varepsilon_{c,lim}$, the model in Model Code 90 [45] was implemented. The resulting combined stress-strain curve is shown by the black curve in Fig. 11(a). It should be noted that Model Code 2010 and Model Code 90 employ the same formulation for describing the ascending branch of the stress-strain relationship. The key difference is that Model Code 2010 relates the strain at maximum stress to the compressive strength, whereas Model Code 90 assumes a constant value. Thus, the descending branch according to Model Code 90 is fully compatible with the Model Code 2010 formulation, provided that $\varepsilon_{c,lim}$ is determined according to Model Code 90 to ensure continuity. However, the descending part of the stress-strain curve depends on the length of the test specimen. Because the model described in Model Code 90 is only suitable for specimens with 200 mm length, the post-peak law must be adjusted whenever the critical fracture-zone length, L_{cr}, differs from this value. This modification was implemented following Eq. (6), proposed by Hanjari et al. [46]. The variables $\Delta\varepsilon_c$ and $\Delta\varepsilon_{c,mod}$, illustrated in Fig. 11(a), represent the original and modified difference between the post-peak strain at a certain stress level and the equivalent strain calculated using the secant module, E_{sec}. The red dashed curve in Fig. 11(a) shows the modified compressive stress-strain relationship used for all beams in the FE model. It was generated under the assumption that the critical compressive zone localises within a single mesh element, i.e. $L_{cr} = 100$ mm. This assumption was verified for all specimens. Finally, the viscosity parameter was set to 1×10^{-5} and all other plasticity parameters were kept at their default values.

$$\Delta\varepsilon_{c,mod} = \Delta\varepsilon_c \cdot \frac{200\ \text{mm}}{L_{cr}} \qquad \text{Eq. (6)}$$

The tensile behaviour of the concrete was defined by a linear-elastic stress-strain relationship up to the mean tensile strength, f_{ctm}, as illustrated in Fig. 11(b). After cracking initiation, the softening behaviour was described with the bilinear stress-crack relationship from Model Code 2010, shown in Fig. 11(c), in which w denotes the crack width. The cracking strain was obtained by dividing w by a smeared length, l_s, equal to the mesh size. The fracture energy, G_F, was estimated using Eq. (7) according to Model Code 2010, in which f_{cm} is given in MPa and G_F in N/m.

$$G_F = 73(f_{cm})^{0.18} = 150\ \text{N}/\text{m} \qquad \text{Eq. (7)}$$

The reinforcing steel was modelled using the classical material model for metal plasticity with a bilinear stress-strain relationship and strain hardening, as illustrated in Fig. 12. The relevant material properties are summarised in Table 2. To represent rebar fracture in a numerically simple and stable manner, the tensile stress was assumed to drop rapidly once the ultimate strain, ε_u, was reached, reducing to 1 MPa at $1.05\varepsilon_u$. Thereafter, the stress was held constant to simulate complete rebar fracture.

4.2. Analytical model

The analytical model consists of two sequential components. The first resolves the response during the CMA phase, and the second evaluates the behaviour during the TMA stage. The two parts are presented separately in the following subsections.

4.2.1. Formulation for the CMA phase

The model presented in this study builds upon the analytical framework proposed by Kang and Tan [20] and later expanded in e.g. Refs. [13,21]. The original formulation was developed to describe the CMA response of beam-column sub-assemblages subjected to a mid-column removal scenario, in which the beams have a rigid core (i.e. the remaining column stub) at midspan. The original model did not account for rebar fracture. This limitation becomes critical for beams with low slenderness or reinforcement with limited ductility, for which rebar fracture is likely to occur during the CMA phase. Hence, the present work adapts the original method for single-span beams and incorporates the ability to predict rebar fracture.

The beam is idealised as two rigid segments connected by a plastic hinge at midspan, with additional plastic hinges at the supports. Plane sections area assumed to remain plane. Rotation is assumed to concentrate at the hinges, while the beam segments undergo elastic axial shortening under the resulting compressive force. The corresponding plastic mechanism is shown in Fig. 13(a). Because the supports are not perfectly rigid, the support's face rotates by an angle α when the beam rotates by θ. The combined effect of rotation

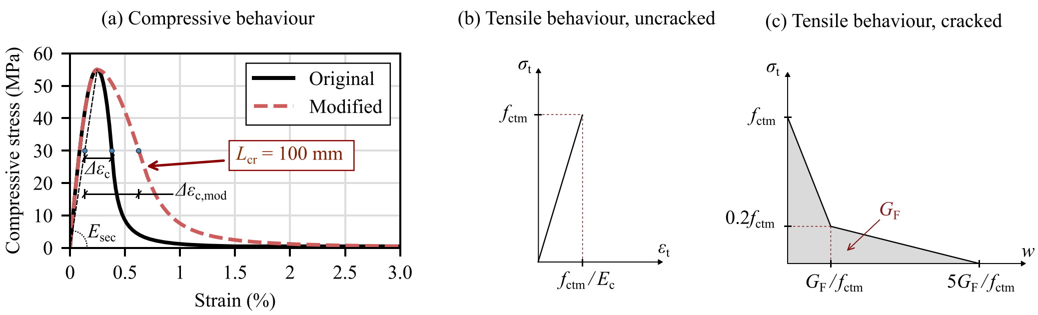

Fig. 11. Stress-strain relationships for concrete in compression and tension for modelling purpose.

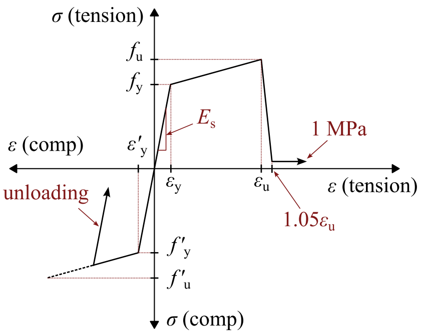

Fig. 12. Stress-strain relationship for reinforcing steel for modelling purpose.

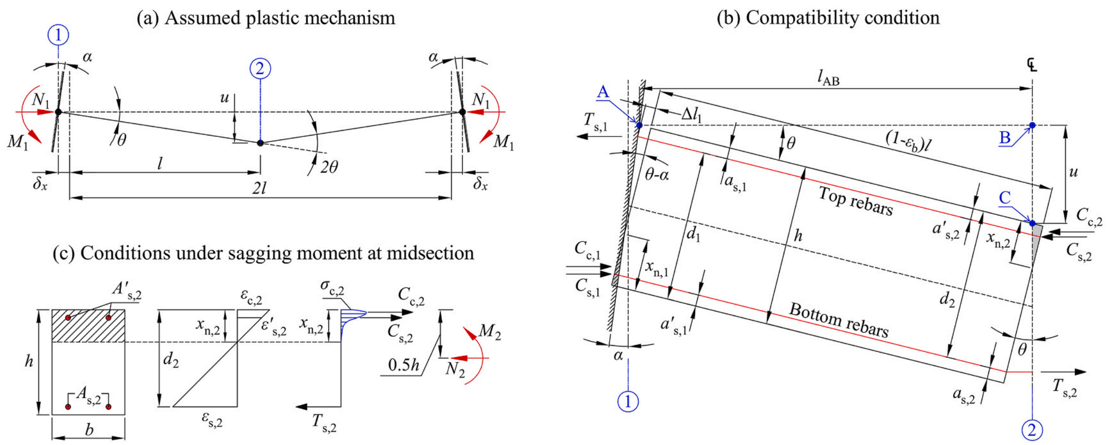

Fig. 13. Geometrical conditions of the restrained beams under three-point bending.

and change in length of the beam also induces a horizontal translation δ_x at the supports.

The original model in Ref. [20] assumes that the strain in the top reinforcement decreases linearly from its maximum value at the yield lines to zero at the point of zero moment. While this assumption is retained for the strain distribution at the supports, the present study introduces a relationship between the curvatures at the support and midspan. This relationship is then used to link the reinforcement strains at the two sections. A key advantage of this approach is that it enables calibration of the onset of rebar fracture at midspan. The curvature κ is defined by Eq. (8), in which ϕ is the rotation at the hinge and L_p is the corresponding plastic hinge length.

$$\kappa = \frac{\phi}{L_p} \quad \text{Eq. (8)}$$

The plastic hinge length *at each side* of the midspan hinge can reasonably be assumed to match the plastic hinge length at the supports, which—via Eq. (8)—would imply equal curvature at midspan and at the supports. This assumption was adopted, for example, in Ref. [32]. In practice, however, effects such as tensile-strain penetration into the column stubs and limited translational or rotational restraint at the BCs tend to reduce the curvature at the supports. The response exhibited by specimen B7 illustrates a case in which the midspan curvature exceeds the support curvature. A plausible upper-bound mechanism is one in which the *total* plastic hinge length at midspan equals that at the supports, resulting in a midspan curvature that is twice as large as the support curvature. The actual behaviour is expected to lie between these two limits. Comparison with the experimental results and FE analyses showed that adopting the midpoint of this interval, as expressed in Eq. (9), provides satisfactory predictions across all specimens. The variables κ_1 and κ_2 denote the curvatures at the support and midspan sections. Although this assumption introduces uncertainty, it is no more uncertain than the original model's assumption concerning distribution of steel strain, while offering the added benefit of enabling calibration of rebar-fracture initiation. Indeed, increasing the ratio κ_2/κ_1 reduces the deflection at which first rebar fracture at the bottom at midspan occurs. Conversely, decreasing this ratio delays the first rebar fracture.

$$\kappa_2 / \kappa_1 = 1.5 \quad \text{Eq. (9)}$$

The original model in Ref. [20] underestimates the steel strain as it assumes a linear strain distribution along the length of the rebars. In reality, the strain distribution is a complex nonlinear function, influenced by bond-slip, cracking and tension stiffening effects. Since the original formulation did not aim to capture rebar fracture, this limitation mainly affected the computed steel stress after yielding and had little impact on the predicted capacity. However, to enable reliable prediction of the rebar fracture, a more realistic approximation of the steel strain is needed. A full implementation of tension stiffening effects would add considerable complexity, exceeding the intended level of simplicity for the model. Instead, a practical solution adopting a reduced strain at maximum load ($\varepsilon_{u,mod}$) was implemented. Comparisons with experimental and FE results showed that calculating $\varepsilon_{u,mod}$ using Eq. (10) consistently provided conservative estimates of the onset of rebar fracture. The assumption in Eq. (10) is similar to the experimental observations by Nozad and Moa [47], who reported that the mean steel strain over the plastic zone at failure of six RC beams subjected to four-point bending was on average 45% of the fracture strain obtained from material testing.

$$\varepsilon_{u,mod} = 0.5\varepsilon_u \quad \text{Eq. (10)}$$

Fig. 13(b) shows the compatibility condition of the beam. The horizontal distance from the support face (point A) to the centre of the beam (point B), l_{AB}, is given by Eq. (11), in which l is the initial distance between the midspan and support hinges. Additionally, the distance between points A and C is given by Eq. (12), in which ε_b denotes the compressive axial strain in the beam, as defined in Eq. (13). Thus, the geometric compatibility condition can be expressed by Eq. (14).

$$l_{AB} = l + \delta_x - 0.5h\tan(\alpha) \quad \text{Eq. (11)}$$

$$l_{AC} = (1-\varepsilon_b)l + \left(h - x_{n,1}\right)\tan(\theta-\alpha) - x_{n,2}\tan(\theta) \quad \text{Eq. (12)}$$

$$\varepsilon_b = \frac{N_C}{bhE_c} \quad \text{Eq. (13)}$$

$$l_{AB} = l_{AC}\cos(\theta) \quad \text{Eq. (14)}$$

Assuming linear-elastic behaviour for the translational restraint, the horizontal reaction force at the support can be obtained from Eq. (15), in which the horizontal reaction force is assumed to be equal the compressive axial force (N_C).

$$N_C = K_T\delta_x \quad \text{Eq. (15)}$$

However, to allow for more complex boundary conditions, the relationship between the horizontal reaction force and the support translation may instead be expressed through a general function g, as given by Eq. (16). Here, g follows the behaviour described in Fig. 9.

$$N_C = g(\delta_x) \quad \text{Eq. (16)}$$

Linear-elastic behaviour is adopted for the rotational restraint. Thus, the reaction moment at the support is calculated with Eq. (17).

$$M_1 = K_R\alpha \quad \text{Eq. (17)}$$

In addition to compatibility requirements, equilibrium conditions must be satisfied at both the support and midspan sections. The force-equilibrium conditions at midspan are illustrated in Fig. 13(c). Equilibrium at the support section is resolved in a similar manner. The sum of forces at these critical sections is given by Eq. (18), in which $C_{c,1}$ and $C_{c,2}$ denote the concrete's compressive resultant, $C_{s,1}$ and $C_{s,2}$ are the forces in the compression reinforcement, and $T_{s,1}$ and $T_{s,2}$ are the forces in the tension reinforcement. Subscript $_1$ refers to the support section, while subscript $_2$ refers to the midspan section. Moment equilibrium around the centroid of the cross-section ($h/2$) results in Eq. (19) and Eq. (20), in which M_1 and M_2, and $\sigma_{c,1}$ and $\sigma_{c,2}$ are the moment and compressive stress in the concrete at the support and midspan, respectively.

$$N_C = C_{c,1} + C_{s,1} - T_{s,1} = C_{c,2} + C_{s,2} - T_{s,2} \quad \text{Eq. (18)}$$

$$M_1 = b\int_0^{x_{n,1}} \left(0.5h - x_{n,1} + y\right)\sigma_{c,1}\,dy + C_{s,1}\left(0.5h - a'_{s,1}\right) + T_{s,1}\left(0.5h - a_{s,1}\right) \quad \text{Eq. (19)}$$

$$M_2 = b\int_0^{x_{n,2}} \left(0.5h - x_{n,2} + y\right)\sigma_{c,2}\,dy + C_{s,2}\left(0.5h - a'_{s,2}\right) + T_{s,2}\left(0.5h - a_{s,2}\right) \quad \text{Eq. (20)}$$

The compressive behaviour of the concrete is assumed to follow the original combined stress-strain relationship from Model Code 2010 and Model Code 90, described by the black curve in Fig. 11(a). The tensile strength of the concrete is disregarded. The behaviour of the reinforcing steel is represented by a bilinear stress-strain relationship with strain-hardening, as illustrated in Fig. 12. However, rebar fracture is not included at this stage. That is, the stress is allowed to continue growing beyond f_u with the same inclination. Unloading from compression into tension in the reinforcement is assumed to follow a linear path governed by the elasticity module, E_s.

To close the formulation, a link is required between the strain in the tension reinforcement and the beam's deflection. At the support section, the strain in the extreme tension reinforcement is assumed to vary linearly from its maximum value to zero at the point of zero moment. Thus, the elongation in the reinforcement, Δl_1, is equivalent to $0.5\varepsilon_{s,1}\lambda_1$. The variable λ_1, determined using Eq. (21), denotes the distance between the support and the point of zero moment. Finally, the relationship between the reinforcement strain at the support, the support rotation θ, and the position of the neutral axis is expressed by Eq. (22).

$$\lambda_1 = \frac{M_1 l}{M_1 + M_2} \quad \text{Eq. (21)}$$

$$\Delta l_1 = 0.5\varepsilon_{s,1}\lambda_1 = \left(h - x_{n,1} - a_{s,1}\right)\tan(\theta - \alpha) \quad \text{Eq. (22)}$$

The relationship between the curvature at the critical sections, given by Eq. (9), is used to derive an expression for the strain in the extreme tension reinforcement at midspan, as given by Eq. (23).

$$\varepsilon_{s,2} = \left(\frac{\kappa_2}{\kappa_1}\right)\varepsilon_{s,1}\frac{d_2 - x_{n,2}}{d_1 - x_{n,1}} = 1.5\varepsilon_{s,1}\frac{d_2 - x_{n,2}}{d_1 - x_{n,1}} \quad \text{Eq. (23)}$$

Finally, the midspan deflection and corresponding load-carrying capacity are calculated according to Eq. (24) and Eq. (25).

$$u = l_{AB}\tan(\theta) \quad \text{Eq. (24)}$$

$$P = \frac{2(M_1 + M_2 - N_C u)}{l} \quad \text{Eq. (25)}$$

It should be noted that a steel plate of width a_{lp} was used to transfer the applied load to the top surface of the test specimens. As the beams deflected, a small gap opened between the underside of the loading plate and the concrete surface. Consequently, the load was transferred to the concrete primarily through contact at the plate's edges. Therefore, a more correct estimation of the applied load could be achieved using Eq. (26). For the tests conducted in this work, the influence of this effect was estimated to be in the order of 5%.

$$P = \frac{2(M_1 + M_2 - N_C u)}{l - 0.5a_{lp}} \quad \text{Eq. (26)}$$

The solution is obtained iteratively by repeating the following steps:

i) Input a support rotation: θ
ii) Equilibrium at the support section: Assume $x_{n,1}$ and M_1. Compute λ_1 and α using Eq. (21) and Eq. (17). To evaluate λ_1, use the value of M_2 from the previous iteration. For the first iteration, $M_2 = M_1$. Determine $\varepsilon_{s,1}$ with Eq. (22). With these quantities, solve equilibrium at the support section to obtain N_1 and an updated value of M_1. For the assumed $x_{n,1}$, repeat this process until M_1 converges.
iii) Equilibrium at the midspan section: After convergence of equilibrium at the support, assume $x_{n,2}$. Compute $\varepsilon_{s,2}$ using Eq. (23). Solve the midspan section to obtain N_2 and M_2. Verify that $N_1 = N_2$. If not, assume a new value of $x_{n,2}$ and repeat until equilibrium is satisfied.
iv) Compatibility condition: Once equilibrium at both section is satisfied, verify compatibility. Calculate ε_b with Eq. (13). The support translation is given by Eq. (15) or Eq. (16). Determine l_{AB} and l_{AC} from Eq. (11) and Eq. (12). Finally, verify that Eq. (14) is fulfilled. If compatibility is not fulfilled, return to step ii), assume a new value of $x_{n,1}$, and repeat the procedure.
v) Deflection and load-carrying capacity: When both equilibrium and compatibility are achieved, calculate the deflection and load-carrying capacity using Eq. (24) and Eq. (25) or Eq. (26).
vi) Update support rotation: Increase the support rotation by a prescribed $\Delta\theta$ and repeat the entire cycle until the target support rotation is reached.

It should be noted that an initial connection gap was observed for all beams in the present study, as discussed in Section 3.3. The original formulation in Ref. [20] accounts for such an initial gap. However, its influence on the overall response was deemed relatively minor. Consequently, although the initial gas was included in the FE model, it was omitted from the analytical model to keep it as simple as possible.

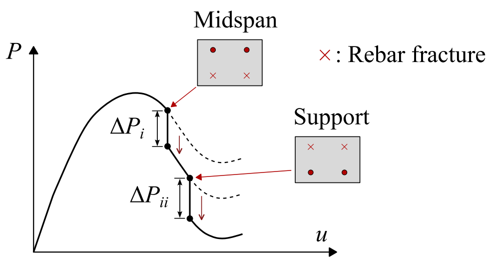

Fig. 14. Illustration of the proposed method for modifying the load-deflection curve during CMA response to account for rebar fracture.

4.2.2. Rebar fracture during CMA response

The development of the reinforcement strain is examined posterior to the evaluation of the CMA response. If reinforcement fracture is confirmed, the load-deflection curve must be adjusted. Reinforcement fracture is assumed to occur at any reinforcement layer where the tensile strain reaches the reduced ultimate strain, $\varepsilon_{\mathrm{u,mod}}$. To resolve equilibrium at the time of reinforcement fracture, the following assumptions are imposed: (i) the membrane force remains unchanged after rebar fracture; and (ii) the curvature at the section remains unchanged. With these conditions, the cross-section can be reanalysed to stablish a new equilibrium state, yielding an updated moment capacity, which is then substituted into Eq. (25) or Eq. (26) to compute a new value of the resistance, P_{new}. To construct the final load-deflection curve in the CMA phase, the original curve is shifted vertically by $\Delta P = P - P_{\mathrm{new}}$ at each fracture event, as illustrated in Fig. 14.

4.2.3. Formulation for the TMA phase

The evaluation of the CMA response is carried out until the membrane force reduces to zero at a midspan deflection u_0. Beyond this point, the response of the beam is treated as TMA. The reinforcement strain values at the end of CMA phase ($\varepsilon_{\mathrm{s,1,CMA}}$, $\varepsilon'_{\mathrm{s,1,CMA}}$, $\varepsilon_{\mathrm{s,2,CMA}}$, $\varepsilon'_{\mathrm{s,2,CMA}}$) serve as initial conditions for computing the membrane force in the subsequent TMA analysis. Although these strain values will generally differ, the subsequent increment of strain is, from this stage onward, assumed to be uniform across all reinforcement layers. To account for tension stiffening effects, the reduced ultimate strain, $\varepsilon_{\mathrm{u,mod}}$—previously implemented in the CMA model—is maintained for the TMA phase.

The TMA model assumes a three-hinged plastic mechanism akin to that in Fig. 13(a). However, the translation as the supports is assumed to be fully rigid and the beam is assumed to rotate freely at the supports. The external load is assumed to be carried entirely by catenary action. Any contribution from the concrete is disregarded. The load-carrying capacity is related to the membrane force and the beam's deflection through global force equilibrium. For any midspan deflection u_i exceeding u_0, the support rotation is given by Eq. (27). The load-carrying capacity and the horizontal reaction force are calculated with Eq. (28) and Eq. (29), in which $N_{\mathrm{T},i}$ is the corresponding tensile membrane force.

$$\theta_i = \operatorname{atan}\left(\frac{u_i}{l}\right) \qquad \text{Eq. (27)}$$

$$P_i = 2N_{\mathrm{T},i}\sin(\theta_i) \qquad \text{Eq. (28)}$$

$$H_i = N_{\mathrm{T},i}\cos(\theta_i) \qquad \text{Eq. (29)}$$

A formulation to estimate $N_{\mathrm{T},i}$ is derived as follows. The initial length at the onset of TMA, l_0, is given by Eq. (30), while the distance between the support hinge and the midspan section, l_i, for a deflection u_i is obtained from Eq. (31). The resulting increase in tensile strain in the reinforcement, $\Delta\varepsilon_{\mathrm{s},i}$, is determined using Eq. (32).

$$l_0 = \sqrt{u_0^2 + l^2} \qquad \text{Eq. (30)}$$

$$l_i = \sqrt{u_i^2 + l^2} \qquad \text{Eq. (31)}$$

$$\Delta\varepsilon_{\mathrm{s},i} = \frac{l_i - l_0}{l_0} \qquad \text{Eq. (32)}$$

It should be noted that Eq. (32) assumes uniform distribution of strains along the entire length of the beam. Using this strain increase directly, in combination with $\varepsilon_{\mathrm{u,mod}}$, still results in overprediction of the deflection at which rebar fracture takes place. One reason for this is that the contribution of bending, which has been neglected in the simplified model, may still be significant at the initial stage of the TMA regime. At very large rotations, the influence of local bending in the reinforcement bars at the hinge regions may also become significant. These effects increase the reinforcement strain at the critical sections. Thus, when calculating the total reinforcement strain at a deflection u_i, a modification factor ξ (≥ 1) is used to adjust $\Delta\varepsilon_{\mathrm{s},i}$. While the modification factor ξ may differ for the tension and compression reinforcement, it is here assumed to be the same for all reinforcement layers. The total strain at the reinforcement layers is then computed using Eq. (33) to Eq. (36). The value of ξ adopted in the present study, determined based on comparisons against the experimental results and FE analyses, is given in Eq. (37).

$$\varepsilon_{\mathrm{s},1,i} = \varepsilon_{\mathrm{s,1,CMA}} + \xi\Delta\varepsilon_{\mathrm{s},i} \qquad \text{Eq. (33)}$$

$$\varepsilon'_{\mathrm{s},1,i} = \varepsilon'_{\mathrm{s,1,CMA}} + \xi\Delta\varepsilon_{\mathrm{s},i} \qquad \text{Eq. (34)}$$

$$\varepsilon_{\mathrm{s},2,i} = \varepsilon_{\mathrm{s,2,CMA}} + \xi\Delta\varepsilon_{\mathrm{s},i} \qquad \text{Eq. (35)}$$

$$\varepsilon'_{\mathrm{s},2,i} = \varepsilon'_{\mathrm{s,2,CMA}} + \xi\Delta\varepsilon_{\mathrm{s},i} \qquad \text{Eq. (36)}$$

$$\xi = 2.0 \qquad \text{Eq. (37)}$$

The tensile forces at the support and midspan sections, $N_{\mathrm{T},1,i}$ and $N_{\mathrm{T},2,i}$, are obtained from Eq. (38) and Eq. (39), in which σ_{s} denotes the stress-strain relationship of the reinforcing steel, which follows the bilinear law with strain hardening illustrated in Fig. 12. As discussed before, $\varepsilon_{u,mod}$ is adopted as the ultimate strain, and the stress is set to zero if the strain exceeds this limit.

$$N_{T,1,i} = A_{s,1}\sigma_s\left(\varepsilon_{s,1,i}\right) + A'_{s,1}\sigma_s\left(\varepsilon'_{s,1,i}\right) \quad \text{Eq. (38)}$$

$$N_{T,2,i} = A_{s,2}\sigma_s\left(\varepsilon_{s,2,i}\right) + A'_{s,2}\sigma_s\left(\varepsilon'_{s,2,i}\right) \quad \text{Eq. (39)}$$

Because no compatibility conditions are enforced at the level of the cross-sections after the onset of TMA, the values of $N_{T,1,i}$ and $N_{T,2,i}$ do not necessarily match. To address this, the effective tensile membrane force in the beam, $N_{T,i}$, is defined as the minimum of these two values, as given by Eq. (40).

$$N_{T,i} = \min\left(N_{T,1,i}, N_{T,2,i}\right) \quad \text{Eq. (40)}$$

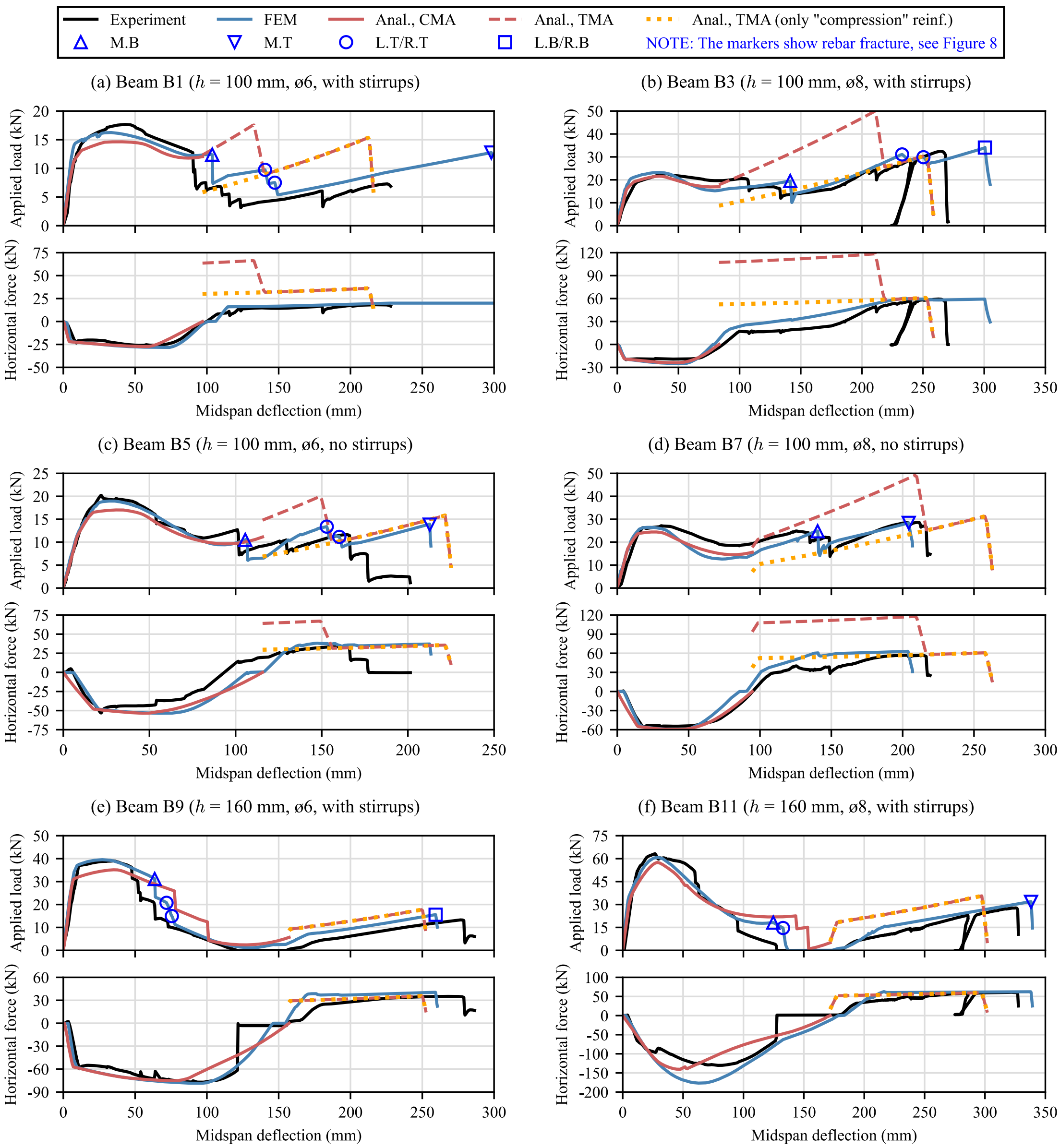

Fig. 15. Comparison between results from the experiments, FE model and analytical approach. The markers indicate reinforcement fracture in the FE model.

4.3. Validation of the models

To assess the performance of the numerical and analytical models, both approaches were applied to predict the response of the test specimens, and the results were compared with the experimental measurements. To account for the asymmetric translational restraints, equivalent stiffness constants $K_{T,1,eq}$ and $K_{T,2,eq}$—calculated using Eq. (41) and Eq. (42)—were used in the analytical CMA model. However, the analytical TMA model assumes zero horizontal displacement at the supports. Hence, deviations from the experimental results are expected for those beams in which the nonlinear behaviour of the BCs at the right support was most pronounced. In the numerical models, asymmetric nonlinear BCs were applied according to the properties listed in Table 4.

$$K_{T,1,eq} = \left[\frac{2K_T K_{T,1}}{K_T + K_{T,1}}\right] \quad \text{Eq. (41)}$$

$$K_{T,2,eq} = \left[\frac{2K_T K_{T,2}}{K_T + K_{T,2}}\right] \quad \text{Eq. (42)}$$

The results are presented in Fig. 15. Overall, the FE model showed good agreement with the experimental data. It accurately predicted the peak CMA resistance and the evolution of the membrane force in both response phases. The largest errors in the prediction of the peak CMA resistance were observed for specimens B1 (8.0%) and B5 (6.2%). Consistent with the experiments, the bottom reinforcement at midspan was the first to fail in all beams (labelled M.B in Figs. 8 and 15). The deflection at first reinforcement fracture was also captured accurately by the FE model in most specimens. The most pronounced difference occurred for B11: in the FE model, fracture of the tension reinforcement at M.B occurred almost simultaneously with that at the supports (labelled L.T/R.T) at approximately 140 mm, whereas in the experiments it occurred independently at around 60 mm.

The FE model also successfully reproduced the loss of capacity caused by the failure of the extreme tension reinforcement during the CMA phase in the beams with $L/h = 12.5$ (B9 and B11). It further captured the deformation at outright collapse for most specimens. The main exception was B1, for which the deformation continued to increase with only a minor rise in reinforcement strain due to the small value of the stiffness constant $K_{T,3}$. This reflects a limitation of the model: it does not properly describe other mechanisms that drive strain growth, such as discrete cracking or local rebar bending.

Notably, in agreement with the experiments, the FE model predicted that the final reinforcement fracture in B3 occurred at the support, and that specimen B7 did not experience any reinforcement failure at the supports. Since the only difference between the FE models of these two specimens lay in the definition of the BCs, this suggests that the BCs influenced the location of reinforcement fracture, which was initially speculated in Section 3.2. While further research is needed to confirm this, these findings appear to indicate that the boundary conditions may influence not only the magnitude of the restraint forces, but also the damage pattern and consequentially the rotational capacity and the locations where reinforcement fracture is most likely to occur.

Finally, the FE model predicted that outright collapse of B9 was triggered by failure of the bottom reinforcement at the support, whereas the experiments showed that collapse of this beam occurred when the top reinforcement at midspan fractured. However, the top reinforcement at midspan was very close to fracture in B9's FE model, suggesting that the variability in the fracture strain (see Fig. 5) may govern the precise location of the final rebar fracture for these conditions.

The analytical model for the CMA phase produced acceptable and conservative predictions of the response, although it consistently underestimated the peak CMA load in all beams. The degree of underestimation varied among specimens, but the predictions remained within a reasonable margin. As with the FE results, the largest discrepancy occurred for beams B1 (22.0%) and B5 (17.0%), indicating consistency between the two modelling approaches in this regard. The analytical model captured the deflection at peak load and the post-peak softening behaviour with good accuracy. For beams with $L/h = 20$, the first rebar fracture was predicted to occur later than observed experimentally, whereas the prediction improved for beams with $L/h = 12.5$. In those deeper beams, the model correctly identified failure of the extreme tension reinforcement during CMA. The proposed simplified approach used to estimate the reduced capacity after rebar fracture also provided results of acceptable accuracy. Notably, the resulting load-deflection curve generated using this approach dropped close to zero, consistent with the experimental observation.

The analytical model for TMA exhibited larger deviations from the experimental results, most notably in beams B1, B3 and B7. The primary source of this discrepancy was the assumption of fully rigid translation in the analytical formulation. As discussed in Section 3.3, the actual supports behaved more flexibly and they could mobilize only a limited horizontal reaction force, which was lower than the tensile force that the reinforcement could theoretically develop. Because of this, TMA could not fully develop in the tests and bending action contributed more significantly to the overall response. Since neither of these effects were represented in the analytical model, it overpredicted the tensile membrane force and delayed the onset of first rebar fracture. A potential workaround is to compute the load-deflection curve utilising only the "compression-side" reinforcement in the TMA calculations, illustrated by the dotted lines in Fig. 15. This approach effectively considers only *secondary* catenary action, producing a response that more closely matches the experimental behaviour. In contrast, the TMA prediction for beam B5 aligned reasonably with the tests and was likely affected by the variability in fracture strain for the ø6-mm rebars. Finally, for B9 and B11, the analytical and experimental results showed good agreement. These results underscore that properly capturing first fracture of the extreme tension reinforcement is essential for reliably describing catenary action.

4.4. Evaluation of the analytical model with ideal BCs

The analytical model was also evaluated with idealised linear-elastic and symmetric boundary conditions using the FE model as the reference solution, given its demonstrated accuracy in Section 4.3. For this analysis, the supports were assumed to have a pure linearly elastic response in both models, and no initial gap was introduced. The BCs were defined using a translational stiffness $K_T = 1.00 \times 10^8$ N/m and rotational stiffness $K_R = 1.00 \times 10^7$ Nm/rad at both supports. These stiffness values were determined by calculating the mean value across all specimens and rounding up to the nearest whole number. It is worth noting that the adopted stiffness values are consistent with the support stiffness constants reported in Ref. [37], in which a similar test setup was used. Because the stirrups have no significance in the simplified FE model, no distinction arises between B1 and B5 or between B3 and B7 with these idealised BCs.

Fig. 16 compares the load-deflection and horizontal force-deflection curves from the analytical model and the FE simulations. Very good agreement between the two approaches was obtained across the overall response. However, the analytical model underestimates the peak CMA resistance in all cases, as also observed in the comparisons in Section 4.3. The discrepancies in the prediction of the peak CMA resistance ranged between 5.3% and 12.0%. Nonetheless, the location of the peak load and the post-peak softening behaviour was well described by the analytical model. The analytical model also correctly captured the rebar fracture events during both the CMA and TMA phase. The overall description of the membrane force by the analytical model was good for the slender beams. However, noticeable underprediction of the membrane force was obtained for the deeper beams. Overall, the analytical model provided robust predictions, capturing the essential features of membrane action. These results indicate that the limitations of the TMA model discussed in Section 4.3 become less relevant when symmetric linear-elastic boundary conditions are assumed.

A discontinuity at the CMA-to-TMA transition is observed in the analytical prediction shown in Fig. 16. This discontinuity arises because the TMA model deliberately neglects the contribution of the concrete and bending capacity. As a result, the axial force predicted by the analytical TMA model does not equal zero at the transition point. In reality, the concrete compressive force would be in equilibrium with the reinforcement's tensile force. At the same time, this non-zero axial force at the onset of the TMA phase compensates for the omission of the bending capacity, thereby enabling a better prediction of the load-carrying capacity under the assumption of pure catenary action. Here, it is recommended to connect the two phases with a straight line, as illustrated by the black dashed lines in Fig. 16. It should also be noted that the effects of neglecting the contribution from bending action decreases with increasing deflection.

5. Discussion

The study experimentally investigated the response of restrained RC beams under three-point bending. All specimens displayed a combined flexural-membrane response, with no evidence of shear cracking. Indeed, no recognizable difference in the overall response was discerned between specimens with and without stirrups. However, the presence of stirrups may become more influential in elements with lower slenderness or higher reinforcement ratios than those examined in the present study.

In general, the initial phase of response was consistent across all specimens: each beam developed an enhanced resistance, P_{CMA}, exceeding the theoretical unrestrained flexural capacity. However, notable differences emerged in the post-peak CMA response and throughout the phase governed by TMA. These differences reflect the influence of the beam slenderness, reinforcement ratio, and reinforcement's fracture strain.

Within the CMA regime, resistance enhancement was most pronounced in the beams with the lowest span-to-depth ratio (B9 and B11, with $L/h = 12.5$). Likewise, among the beams with $L/h = 20$, greater enhancement was observed in those with lower reinforcement ratio (B1 and B5). These observations indicate an inverse relationship between resistance enhancement and both span-to-depth ratio and reinforcement ratio. These findings are consistent with the experimental results of Su et al. [18], who also reported an inverse correlation between these parameters. Further support comes from Smith [2], who recorded even lower enhancement in symmetrically reinforced slab strips with $L/h > 31$ and $\rho > 0.34\%$, reinforcing the conclusion that resistance enhancement decreases with increasing slenderness. Conversely, for slab strips with $\rho < 0.21\%$, Smith [2] documented enhancement levels greater than those observed in B9 and B11. This supports the conclusion that beams with low reinforcement ratios tend to benefit more from CMA.

In addition to exhibiting the greatest resistance enhancement, the beams with the lower span-to-depth ratios also showed the largest contribution from CMA to the total strain energy. In these specimens, more than 65% of the total strain energy was dissipated during the CMA phase. Furthermore, these beams experienced a rapid post-peak drop in capacity triggered by fracture of the extreme tension reinforcement at midspan and the supports. Consequently, only *secondary* TMA could be mobilised once the tests were resumed. This behaviour highlights the importance of accurately capturing the CMA response in such beams, as it governs both peak resistance and overall energy absorption capacity.

The contribution of CMA to the strain energy was also dominant in beams with low reinforcement ratios. In contrast, the contribution of TMA dominated only in the more slender beams with higher reinforcement ratios ($\rho > 0.66\%$). Smith [2] reported that, on average, 68% of the total energy dissipated in their tests was attributed to TMA, leading to the conclusion that TMA governed the collapse resistance. However, the specimens in Smith's study were considerably more slender than those tested here. Notably, only two of their specimens exhibited greater energy absorption during the CMA phase, both characterised by the lowest reinforcement ratio ($\rho = 0.20\%$).

A sudden post-peak drop in resistance in restrained specimens with low span-to-depth ratios has also been reported in previous studies. One example is Su et al. [18], who attributed this sudden drop to concrete crushing. In their tests, no reinforcement fracture occurred during the CMA phase due to the reinforcement's large fracture strain (> 26%). A similar sudden decline in capacity may also

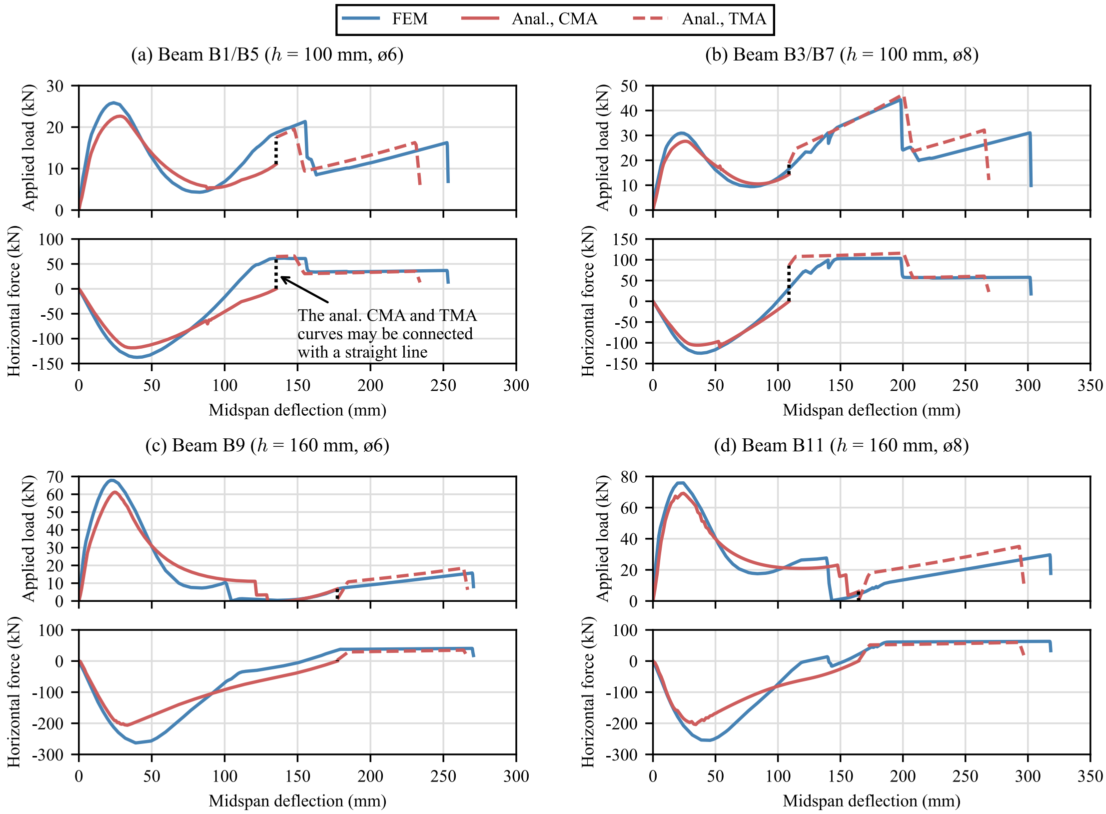

Fig. 16. Comparison between results from the FE model and the analytical approach when assuming idealised linear-elastic boundary conditions.

be triggered by a shear mechanism, as documented in Refs. [15] and [34]. However, in those studies, the load-carrying capacity recovered after the initial drop, allowing tensile membrane forces to develop. Together with the findings of the present study, these results indicate that beams with low span-to-depth ratios are prone to sudden loss of capacity soon after the peak resistance. This phenomenon could be driven by concrete crushing, reinforcement fracture, or shear cracking. However, if caused by fracture of the tension reinforcement, the response may involve an instability mechanism, leading to a temporarily loss of load-carrying capacity.

Reinforcement fracture within the CMA phase in elements with large span-to-depth ratios has also been reported in the literature. For instance, in Refs. [37] and [34] some specimens with $L/h = 23$ experienced fracture of the bottom reinforcement at midspan during the CMA phase. These specimens had a bottom reinforcement ratio of 0.49%. In comparison, the specimens in the present study that reached the onset of TMA with all reinforcement intact had $\rho = 0.66\%$. FarhangVesali et al. [33] similarly reported rebar fracture within the CMA phase in specimens with $L/h = 24.4$. However, in that case, it was triggered by the limited ductility of the reinforcement ($\varepsilon_u = 3.8\%$). This indicates that the rebar fracture within the CMA phase in slender elements may be associated with either low reinforcement ratios or limited reinforcement ductility.

Therefore, fracture of one or all extreme tension reinforcement layers may occur during the CMA regime under certain conditions. Beams with low span-to-depth ratios and low reinforcement ratios are particularly susceptible to this phenomenon. Despite this, reinforcement fracture during the CMA phase in not explicitly considered in most existing analytical models. This underscores both the relevance of the present study and the practical value of the proposed simplified methodology for capturing early rebar fracture.

It is also of interest to examine the deflection at P_{CMA}. In the specimens with $L/h = 20$, the peak CMA resistance was achieved, on average, at a normalised deflection of $u_{CMA} = 0.36h$. In contrast, in the specimens with $L/h = 12.5$, the corresponding value was $u_{CMA} = 0.18h$. This indicates an inverse relationship between the span-to-depth ratio and u_{CMA}. This trend is consistent with the findings of Su et al. [18], who reported average values of $u_{CMA} = 0.31h$ for $L/h = 19$ and $u_{CMA} = 0.21h$ for $L/h \leq 14$. This suggests that the deflection at peak CMA resistance in restrained RC beams and one-way slabs is generally lower than the commonly assumed value for two-way slabs (0.5h). This value was originally proposed by Park and Gamble [1], although the authors noted that one-way slabs are expected to reach peak CMA resistance at smaller deflections.

6. Conclusions

The present study investigated membrane action in longitudinally and rotationally RC beams subjected to three-point bending. The principal findings are summarised below:

- All specimens exhibited combined flexural and membrane action, with CMA behaviour enabling a peak resistance exceeding the theoretical unrestrained flexural capacity. This enhancement decreased with increasing span-to-depth ratios and reinforcement ratios.
- The boundary conditions exhibited a nonlinear response due to unexpected slip between the reaction frames and the floor under high reaction forces. However, a complete characterisation of the boundary conditions was achieved by integrating DIC measurements with data recorded by the load cells.
- The more slender beams with reinforcement with larger fracture strain were able to mobilize *primary* catenary action after completing the snap-through response without experiencing prior reinforcement fracture. In contrast, beams with lower slenderness or lower fracture strain were prone to a rapid post-peak loss of capacity and early rebar fracture within the CMA phase, which limited the utilization of the capacity in the TMA phase. These findings highlight the need for simplified prediction models capable of accurately capturing early reinforcement fracture.
- In more slender beams with higher-ductility reinforcement, the TMA phase provided the largest contribution to the overall energy absorption capacity. In contrast, the CMA phase dominated in beams with low slenderness or low reinforcement ratios. Therefore, for such beams, accurate description of the CMA response is essential for reliable estimation of the internal strain energy. Moreover, the results indicate that the TMA phase may not offer a dependable source of reserve capacity in beams with low slenderness or low reinforcement ratios.
- A simplified FE model and an analytical approach for predicting the full load-deflection curve were implemented and validated. The FE model showed very good agreement with the experimental results, accurately describing the peak CMA resistance and the onset of reinforcement fracture. The analytical approach provided reasonable predictions compared with the experiments. However, it tended to underpredict the peak CMA resistance and, in some cases, delayed the first reinforcement fracture, resulting in overestimation of the TMA capacity. These discrepancies primarily arose from the simplified representation of the boundary conditions in the analytical formulation. Nonetheless, the analytical model performed well under idealised linear-elastic boundary conditions, demonstrating that it is fundamentally sound when its underlying assumptions regarding boundary conditions are satisfied.

It should be noted that the study examined exclusively symmetrically reinforced beams with continuous reinforcement fully anchored at the supports. Consequently, further research is required to extend the findings to specimens with curtailed or lapped reinforcement, as well as beams with asymmetric reinforcement layouts. For the same reasons, the simplified models presented here should be expanded and validated for RC beams with varying reinforcement amounts and discontinuous reinforcement detailing. In addition, the investigation considered only beams subjected to three-point bending. Alternative loading configurations or reinforcement arrangements may activate different plastic mechanisms and should therefore be explored in future work.

CRediT authorship contribution statement

Fabio Lozano: Conceptualization, Formal analysis, Investigation, Methodology, Software, Validation, Visualization, Writing – original draft. **Morgan Johansson:** Conceptualization, Funding acquisition, Methodology, Project administration, Supervision, Writing – review & editing. **Joosef Leppänen:** Conceptualization, Funding acquisition, Methodology, Project administration, Supervision, Writing – review & editing. **Mario Plos:** Conceptualization, Methodology, Supervision, Writing – review & editing.

Declaration of competing interest

The authors declare that they have no known competing financial interests or personal relationships that could have appeared to influence the work reported in this paper.

Acknowledgments

This work was financed by the Swedish Transport Administration; the Swedish Fortifications Agency; and the Swedish Civil Contingencies Agency. The authors are grateful for their support.

The authors would like to thank senior research engineers Sebastian Almfeldt (MSc) and Anders Karlsson (MSc) from Chalmers University of Technology for their expertise and guidance in designing the test rig and conducting the tests.

Data availability

Data will be made available on request.

References

[1] R. Park, W.L. Gamble, Reinforced Concrete Slabs, second ed., John Wiley & Sons, New York, 2000.
[2] P.P. Smith, An Investigation into Tensile Membrane Action as a Means of Emergency Load Redistribution, University of Southampton, 2016. Ph.D. Thesis.
[3] T. Krauthammer, Modern Protective Structures, Taylor & Francis Group, 2008.
[4] A.J. Ockleston, Load tests on a three storey reinforced concrete building in Johannesburg, The Institution of Structural Engineers 33 (1955).

[5] R. Park, The ultimate strength and long-term behaviour of uniformly loaded, two-way concrete slabs with partial lateral restraint at all edges, Mag. Concr. Res. 16 (1964) 139–152, https://doi.org/10.1680/macr.1964.16.48.139.
[6] R. Park, Ultimate strength of rectangular concrete slabs under short-term uniform loading with edges restrained against lateral movement, Proc. Inst. Civ. Eng. 28 (1964) 125–150, https://doi.org/10.1680/iicep.1964.10109.
[7] R. Park, Tensile membrane behaviour of uniformly loaded rectangular reinforced concrete slabs with fully restrained edges, Mag. Concr. Res. 16 (1964) 39–44, https://doi.org/10.1680/macr.1964.16.46.39.
[8] W.A. Keenan, Strength and Behavior of Restrained Reinforced Concrete Slabs Under Static and Dynamic Loadings, Naval Civil Engineering Laboratory, Port Hueneme, 1969.
[9] M.S. Black, Ultimate strength study of two-way concrete slabs, J. Struct. Div. 101 (1975) 311–324, https://doi.org/10.1061/JSDEAG.0003976.
[10] T. Thienpont, W. De Corte, R. Van Coile, R. Caspeele, Compressive membrane action in axially restrained hollow core slabs: experimental investigation, Struct. Concr. 23 (2022) 3007–3020, https://doi.org/10.1002/suco.202100684.
[11] S.-B. Kang, K.H. Tan, Behaviour of precast concrete beam–column sub-assemblages subject to column removal, Eng. Struct. 93 (2015) 85–96, https://doi.org/10.1016/j.engstruct.2015.03.027.
[12] P. Ren, Y. Li, X. Lu, H. Guan, Y. Zhou, Experimental investigation of progressive collapse resistance of one-way reinforced concrete beam–slab substructures under a middle-column-removal scenario, Eng. Struct. 118 (2016) 28–40, https://doi.org/10.1016/j.engstruct.2016.03.051.
[13] S.-B. Kang, S. Wang, S. Gao, Analytical study on one-way reinforced concrete beam-slab sub-structures under compressive arch action and catenary action, Eng. Struct. 206 (2020) 110032, https://doi.org/10.1016/j.engstruct.2019.110032.
[14] J. Jiang, H. Qi, Y. Lu, G.-Q. Li, W. Chen, J. Ye, A state-of-the-art review on tensile membrane action in reinforced concrete floors exposed to fire, J. Build. Eng. 45 (2022) 103502, https://doi.org/10.1016/j.jobe.2021.103502.
[15] L. Cui, X. Zhang, H. Hao, Experimental investigation of resistance function of RC beam considering membrane effects, Eng. Struct. 267 (2022) 114602, https://doi.org/10.1016/j.engstruct.2022.114602.
[16] F.A. Shaik, S.P. Vasudevan, B. Balakrishnan, B. Novák, Investigation of tensile membrane action in reinforced concrete beam-slab systems under combined failure, Eng. Struct. 346 (2026) 121663, https://doi.org/10.1016/j.engstruct.2025.121663.
[17] Y. Jiang, J. Qi, H. Zhou, Y. Tian, X. Cao, Progressive collapse mechanism and resistance calculation of curved concrete beam-column substructure, Eng. Struct. 349 (2026) 121838, https://doi.org/10.1016/j.engstruct.2025.121838.
[18] Y. Su, Y. Tian, X. Song, Progressive collapse resistance of axially-restrained frame beams, ACI Struct. J. 106 (2009), https://doi.org/10.14359/51663100.
[19] CEN, EN 1992-1-1:2004, Eurocode 2: Design of Concrete Structures - Part 1-1: General Rules and Rules for Buildings, 2004.
[20] S.-B. Kang, K.H. Tan, Analytical model for compressive arch action in horizontally restrained beam-column subassemblages, ACI Struct. J. 113 (2016), https://doi.org/10.14359/51688629.
[21] S.-B. Kang, K.H. Tan, Analytical study on reinforced concrete frames subject to compressive arch action, Eng. Struct. 141 (2017) 373–385, https://doi.org/10.1016/j.engstruct.2017.03.039.
[22] X. Lu, K. Lin, C. Li, Y. Li, New analytical calculation models for compressive arch action in reinforced concrete structures, Eng. Struct. 168 (2018) 721–735, https://doi.org/10.1016/j.engstruct.2018.04.097.
[23] S. Wang, S.-B. Kang, Q.-L. Fu, J. Ma, P. Ziolkowski, Analytical approach for membrane action in laterally-restrained reinforced concrete square slabs under uniformly distributed loads, J. Build. Eng. 41 (2021) 102427, https://doi.org/10.1016/j.jobe.2021.102427.
[24] J. Yu, K.H. Tan, Analytical model for the capacity of compressive arch action of reinforced concrete sub-assemblages, Mag. Concr. Res. 66 (2014) 109–126, https://doi.org/10.1680/macr.13.00217.
[25] Y.-J. Zhu, M. Zhou, J.-M. Zhu, X. Nie, Analytical models for load capacities of variable thickness reinforced concrete slabs considering compressive membrane action and boundary effects, Eng. Struct. 246 (2021) 113067, https://doi.org/10.1016/j.engstruct.2021.113067.
[26] W. Chen, J. Cai, J. Huang, X. Yang, J. Ma, Resistance behaviours of clamped HFR-LWC beam using membrane approach, Int. J. Concr. Struct. Mater. 18 (2024) 13, https://doi.org/10.1186/s40069-023-00652-x.
[27] DOD, UFC 3-340-02, Structures to Resist the Effects of Accidental Explosions, 2008.
[28] M. Colombo, P. Martinelli, M. di Prisco, A design approach to evaluate the load-carrying capacity of reinforced concrete slabs considering tensile membrane action, Struct. Eng. Int. 31 (2021) 260–270, https://doi.org/10.1080/10168664.2020.1747957.
[29] I. Burgess, Yield-line plasticity and tensile membrane action in lightly-reinforced rectangular concrete slabs, Eng. Struct. 138 (2017) 195–214, https://doi.org/10.1016/j.engstruct.2017.01.072.
[30] A.T. Pham, K.H. Tan, A simplified model of catenary action in reinforced concrete frames under axially restrained conditions, Mag. Concr. Res. 69 (2017) 1115–1134, https://doi.org/10.1680/jmacr.17.00009.
[31] A. Monserrat-López, A. Nogales Arroyo, D.M. Viula Faria, F. Brantschen, M. Fernández Ruiz, Membrane effects in reinforced concrete: from experimental evidence to numerical and analytical modelling, Eng. Struct. 347 (2026) 121710, https://doi.org/10.1016/j.engstruct.2025.121710.
[32] L. Cui, X. Zhang, H. Hao, Q. Kong, Improved resistance functions for RC elements accounting for compressive and tensile membrane actions, Eng. Struct. 251 (2022) 113549, https://doi.org/10.1016/j.engstruct.2021.113549.
[33] N. FarhangVesali, H. Valipour, B. Samali, S. Foster, Development of arching action in longitudinally-restrained reinforced concrete beams, Constr. Build. Mater. 47 (2013) 7–19, https://doi.org/10.1016/j.conbuildmat.2013.04.050.
[34] J. Yu, K.H. Tan, Structural behavior of RC beam-column subassemblages under a middle column removal scenario, J. Struct. Eng. 139 (2013) 233–250, https://doi.org/10.1061/(ASCE)ST.1943-541X.0000658.
[35] H. Valipour, N. FarhangVesali, S. Foster, A generic model for investigation of arching action in reinforced concrete members, Constr. Build. Mater. 38 (2013) 742–750, https://doi.org/10.1016/j.conbuildmat.2012.09.046.
[36] H.R. Valipour, S.J. Foster, Finite element modelling of reinforced concrete framed structures including catenary action, Comput. Struct. 88 (2010) 529–538, https://doi.org/10.1016/j.compstruc.2010.01.002.
[37] J. Yu, K.-H. Tan, Experimental and numerical investigation on progressive collapse resistance of reinforced concrete beam column sub-assemblages, Eng. Struct. 55 (2013) 90–106, https://doi.org/10.1016/j.engstruct.2011.08.040.
[38] X. Long, B.T. Ketekun, P.M. Iyela, Multiscale analysis of progressive collapse resistance in RC beam-slab sub-assemblages under tensile membrane action, J. Build. Eng. 118 (2026) 115101, https://doi.org/10.1016/j.jobe.2025.115101.
[39] O. Ghunaim, B. El-Ariss, S. Elkholy, Enhanced catenary action prediction of RC structures through improved steel bar material model, Results Eng. 30 (2026) 109980, https://doi.org/10.1016/j.rineng.2026.109980.
[40] Dassault Systèmes, Abaqus 2024 Analysis User's Guide, Dassault Systèmes Simulia Corp, Vélizy-Villacoublay, 2024.
[41] Fib, Fib Model Code for Concrete Structures 2010, International Federation for Structural Concrete, Lausanne, 2013.
[42] K. Qian, D.-F. Wang, T. Huang, Y.-H. Weng, Initial damage and residual behavior of RC beam-slab structures following sudden column removal - numerical study, Structures 36 (2022) 650–664, https://doi.org/10.1016/j.istruc.2021.12.036.
[43] A.T. Pham, K.H. Tan, J. Yu, Numerical investigations on static and dynamic responses of reinforced concrete sub-assemblages under progressive collapse, Eng. Struct. 149 (2017) 2–20, https://doi.org/10.1016/j.engstruct.2016.07.042.
[44] A. Mathern, J. Yang, A practical finite element modeling strategy to capture cracking and crushing behavior of reinforced concrete structures, Materials 14 (2021) 506, https://doi.org/10.3390/ma14030506.
[45] Comite Euro-International du Beton, CEB-FIP Model Code 1990, Redwood Books, Trowbridge, Wiltshire, 1993.
[46] K.Z. Hanjari, P. Kettil, K. Lundgren, Modelling the structural behaviour of frost-damaged reinforced concrete structures, Struct. Infrastruct. Eng. 9 (2013) 416–431, https://doi.org/10.1080/15732479.2011.552916.
[47] A. Nozad, S. Moa, Average Reinforcement Strain in Reinforced Concrete Structures Loaded Until Failure, Chalmers University of Technology, 2021. M.Sc. Thesis.